Neuron

Article

Early molecular layer interneuron hyperactivity triggers Purkinje neuron degeneration in SCA1

Highlights

- Increased molecular layer interneuron (MLIN) activity drives SCA1 pathophysiology
- Inhibition of MLIN ameliorates network and behavioral SCA1 phenotypes
- Mimicking MLIN hyperexcitability in healthy mice generates SCA1-like pathophysiology
- MLIN hyperexcitability is conserved in human SCA1 patient-derived GABAergic neurons

Authors

Federica Pilotto, Christopher Douthwaite, Rim Diab, ..., Benoît Zuber, Sabine Liebscher, Smita Saxena

Correspondence

sabine.liebscher@med.uni-muenchen.de (S.L.), smita.saxena@dbmr.unibe.ch (S.S.)

In brief

Pilotto et al. identify early hyperexcitability of molecular layer interneurons (MLINs) in SCA1 driving circuit dysfunction and motor deficits. Inhibition of MLINs in SCA1 mice induced lasting improvements of circuit pathology and behavior. MLIN proteomics revealed a signature accounting for hyperexcitability, conserved in patient-derived GABAergic neurons.

Pilotto et al., 2023, Neuron *111*, 2523–2543
August 16, 2023
https://doi.org/10.1016/j.neuron.2023.05.016

CellPress

Neuron

CellPress
OPEN ACCESS

Article

Early molecular layer interneuron hyperactivity triggers Purkinje neuron degeneration in SCA1

Federica Pilotto,[1,2,10] Christopher Douthwaite,[3,10] Rim Diab,[1,2] XiaoQian Ye,[3] Zahraa Al qassab,[1,2] Christoph Tietje,[3] Meriem Mounassir,[3] Adolfo Odriozola,[4] Aishwarya Thapa,[1,2] Ronald A.M. Buijsen,[7] Sophie Lagache,[8] Anne-Christine Uldry,[8] Manfred Heller,[8] Stefan Müller,[9] Willeke M.C. van Roon-Mom,[7] Benoît Zuber,[4] Sabine Liebscher,[3,5,6,*] and Smita Saxena[1,2,11,*]

[1]Department of Neurology, Inselspital University Hospital, Bern, Switzerland
[2]Department for BioMedical Research, University of Bern, Bern, Switzerland
[3]Institute of Clinical Neuroimmunology, Klinikum der Universität München, Ludwig-Maximilians University Munich, Martinsried, Germany
[4]Institute of Anatomy, University of Bern, Bern, Switzerland
[5]Munich Cluster for Systems Neurology (SyNergy), Munich, Germany
[6]University Hospital Cologne, Deptartment of Neurology, Cologne, Germany
[7]Department of Human Genetics, Leiden University Medical Center, Leiden, the Netherlands
[8]Proteomics and Mass Spectrometry Core Facility, Department for BioMedical Research, University of Bern, Bern, Switzerland
[9]Flow Cytometry and Cell sorting, Department for BioMedical Research, University of Bern, Bern, Switzerland
[10]These authors contributed equally
[11]Lead contact
*Correspondence: sabine.liebscher@med.uni-muenchen.de (S.L.), smita.saxena@dbmr.unibe.ch (S.S.)
https://doi.org/10.1016/j.neuron.2023.05.016

SUMMARY

Toxic proteinaceous deposits and alterations in excitability and activity levels characterize vulnerable neuronal populations in neurodegenerative diseases. Using *in vivo* two-photon imaging in behaving spinocerebellar ataxia type 1 (*Sca1*) mice, wherein Purkinje neurons (PNs) degenerate, we identify an inhibitory circuit element (molecular layer interneurons [MLINs]) that becomes prematurely hyperexcitable, compromising sensorimotor signals in the cerebellum at early stages. Mutant MLINs express abnormally elevated parvalbumin, harbor high excitatory-to-inhibitory synaptic density, and display more numerous synaptic connections on PNs, indicating an excitation/inhibition imbalance. Chemogenetic inhibition of hyperexcitable MLINs normalizes parvalbumin expression and restores calcium signaling in *Sca1* PNs. Chronic inhibition of mutant MLINs delayed PN degeneration, reduced pathology, and ameliorated motor deficits in *Sca1* mice. Conserved proteomic signature of *Sca1* MLINs, shared with human SCA1 interneurons, involved the higher expression of FRRS1L, implicated in AMPA receptor trafficking. We thus propose that circuit-level deficits upstream of PNs are one of the main disease triggers in SCA1.

INTRODUCTION

The mechanisms underlying the major neurodegenerative diseases (NDs) are still poorly understood. An enigmatic but uniform finding in patients and murine models of NDs is the early alteration in excitability of vulnerable neuronal populations and changes in the corresponding neuronal circuitry.[1,2] For instance, in spinal muscular atrophy, motoneurons (MNs) become hyperexcitable,[3] whereas in amyotrophic lateral sclerosis, spinal MNs become hypoexcitable, losing their ability to fire repetitively.[4,5] Similarly, in spinocerebellar ataxia type-1 (SCA1) and type-2 (SCA2), Purkinje neurons (PNs) show a reduction in the firing rate at presymptomatic stages.[6,7] The precise cause of these alterations and whether they are involved in the degenerative process remains unknown.

SCA1 is a devastating, incurable ND due to the expansion of a polyglutamine (PolyQ) repeat within the ubiquitously expressed protein Ataxin-1, leading to the premature degeneration of cerebellar PNs.[8] One critical open question is why cerebellar PNs selectively degenerate in SCA1. In most NDs, multiple cell types within neuronal circuits throughout the CNS are affected, and crucial synaptic and network dysfunction might occur before the appearance of overt pathology.[9–11] Moreover, it has been increasingly acknowledged that non-cell autonomous impairments, such as early circuit-mediated alterations, might critically govern or even trigger the pathology in disease-vulnerable neurons.[12] Previous studies by us and others highlighted the importance of early circuit-related changes within the cerebellum that affect PN activity in SCA1.[6,13,14] Mainly, excitatory synaptic inputs onto PNs from climbing fibers (CFs), but not from parallel fibers (PFs), are altered presymptomatically, leading to reduced CF-PN synaptic strength and subsequent alterations in PN excitability. This suggests the existence of early, selectively vulnerable circuit components, upstream of the affected PNs.[6,14–16] Most

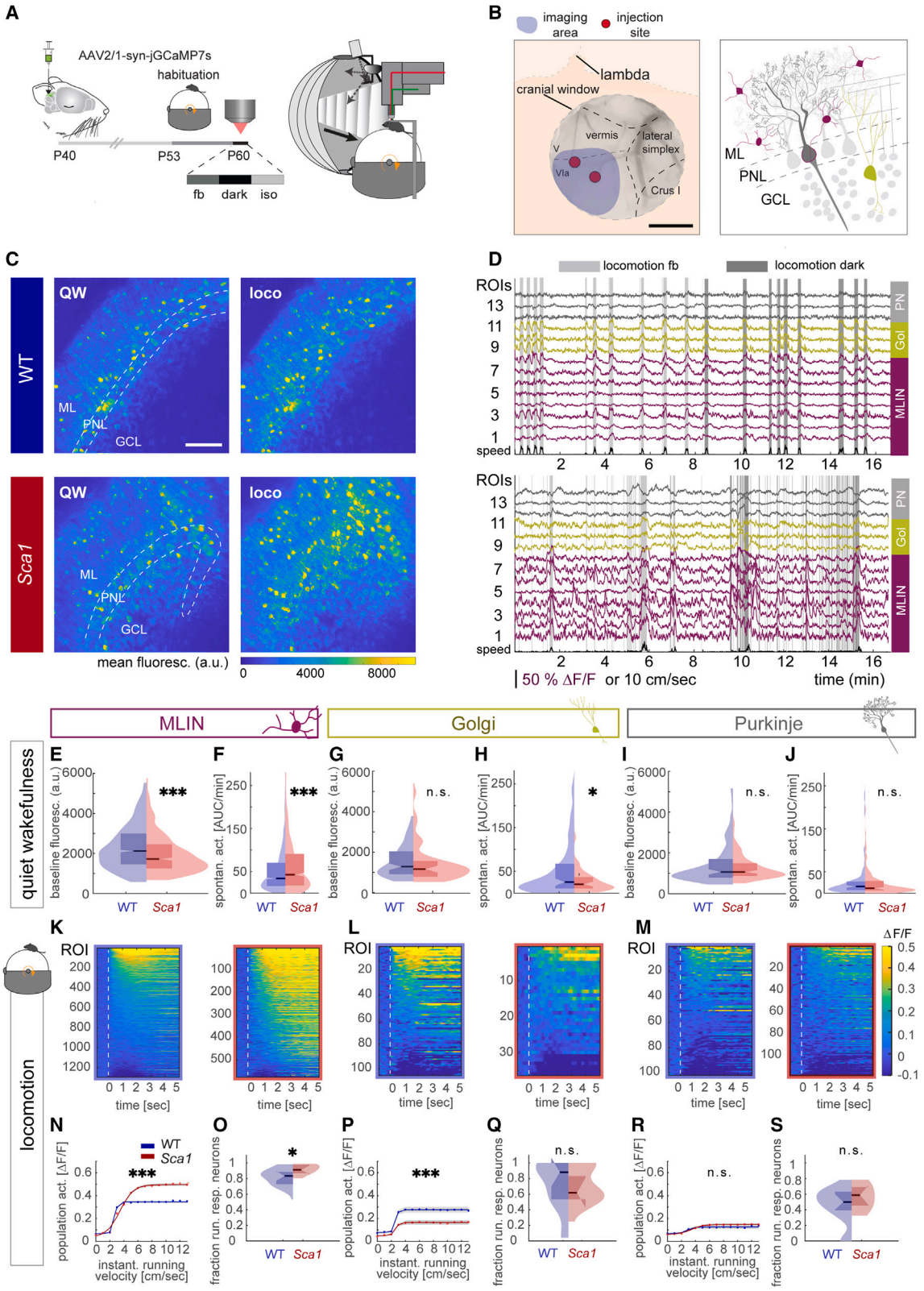

(legend on next page)

previous studies were, however, conducted in slice cultures, allowing only limited insight into how cerebellar circuit elements and entire networks are affected in a spatiotemporal manner in animals by these described molecular and synaptic alterations.

We hypothesized that PolyQ-repeat expansions have a more widespread impact on cerebellar circuits, thereby altering excitatory/inhibitory (E/I) balance, compromising sensorimotor functions, and ultimately triggering PN degeneration. Notably, PN activity is tightly shaped by GABAergic inhibitory molecular layer interneurons (MLINs).[17] Although MLINs do not degenerate in SCA1,[18] they might still contribute to PN degeneration. First *in vitro* evidence for an involvement of MLINs in SCA1 pathology was provided by Edamakanti and colleagues, who identified the hyperproliferation of mutant cerebellar stem cells, preferentially differentiating into GABAergic interneurons, thus enhancing GABAergic synaptic inputs onto PNs.[13] However, the longitudinal molecular, cellular, and circuit-level consequences of such synaptic alterations remain unclear.

Here, combining *in vivo* two-photon calcium imaging in behaving knockin mice, harboring an expansion of 154 CAG repeats in the endogenous *Ataxin-1* mouse locus (termed *Sca1* throughout) together with chemogenetics, histological, ultrastructural, and MLIN-specific proteomic analyses, we demonstrate that neurons within the cerebellar network are differentially affected by the PolyQ expansion. Early impairments mainly involve alterations in the MLIN population, rendering them hyperexcitable, thereby affecting their response properties and compromising coding space in mice. Additionally, MLIN-selective proteomics from *Sca1* mice revealed a disease-linked molecular signature, accounting for the observed changes in mutant MLIN functionality. Notably, this signature was conserved within human SCA1 patient-derived GABAergic neurons. Our results thus indicate that at the circuit level, molecular changes within mutant MLINs govern early cerebellar network dysfunction, promoting PNs degeneration in SCA1.

RESULTS

Cerebellar neuronal activity levels are differentially altered in early symptomatic *Sca1* mice

To assess circuit-level deficits during the early symptomatic phase in postnatal (P) day 60 *Sca1* mice, we performed two-photon calcium imaging in behaving mice, running on a spherical treadmill (Figures 1A and S1). By expressing the genetically encoded calcium indicator GCaMP7s, we simultaneously monitored activity of the three main inhibitory neuronal subtypes in the cerebellar cortex, namely, MLINs, PNs, and morphologically putative Golgi cells (GoI), while mice were maneuvering in a virtual environment (VR), with the locomotion speed being represented by the visual flow of the VR (feedback [fb]) or running in darkness (Figures 1A and 1B). These recordings revealed differential impairments of baseline fluorescence (indicative of alterations in resting cytoplasmic calcium concentrations), neuronal activity levels, and response properties of the different neuronal types (Figures 1C and 1D). As the typical instantaneous firing rate of these cell types exceeds the temporal resolution of the calcium indicator, but the fluorescence signal still scales with overall neuronal firing,[19,20] we assessed neuronal activity by computing the area under curve of the ΔF/F trace. We found that MLINs in *Sca1* mice had not only a significantly lower baseline fluorescence (Figure 1E) but were also more active during quiet wakefulness (QW) during fb and darkness (Figure 1F). Conversely, we did not observe any changes in baseline fluorescence and a decrease in spontaneous neuronal activity levels (i.e., neuronal activity occurring during stationary epochs, measured as area under the curve [AUC]/min) during QW in GoI (Figures 1G and 1H) or PNs (Figures 1I and 1J). Moreover, we found a strong increase in the response to locomotion (Figures 1K–1M) selectively in MLINs in *Sca1* (Figure 1N) and more MLINs being running responsive (Figure 1O). In contrast to MLIN hyperresponsiveness, GoI in *Sca1* were driven less by locomotion (Figure 1P) and displayed no change in the fraction of running responsive neurons (Figure 1Q). At this early disease stage, no alterations in the response to locomotion in PNs was detected (Figures 1R and 1S). However, the number of GoI and PNs captured in this study are considerably lower than those of MLINs; thus, we may potentially underestimate alterations of these neuronal populations.

Recording the same neurons under anesthesia further corroborated these findings (Figures S2A–S2D). We found a strong reduction in the baseline fluorescence of MLINs in *Sca1* mice (Figure S2E), whereas baseline fluorescence was neither altered in GoI (Figure S2F) nor PNs (Figure S2G). We again observed an increase in spontaneous neuronal activity of MLINs (Figure S2H)

Figure 1. Simultaneous monitoring of diverse cerebellar neuronal subtypes in behaving mice

(A) Experimental design (fb, feedback; dark, darkness; iso, isoflurane anesthesia).

(B) Scheme, depicting sites of adeno-associated virus (AAV)-injection and imaging and the cerebellar cortex layers.

(C) Average projection of a quiet wakefulness (QW, left) episode and locomotion (loco, right) of the same field of view (FOV) in WT and *Sca1* mice (dashed lines-cerebellar layers).

(D) Calcium traces of molecular layer interneurons (MLINs, magenta), GoI (GoI, yellow), and Purkinje neurons (PNs, gray) during fb and darkness in WT (upper) and *Sca1* mice (lower). Gray areas-locomotion epochs.

(E–J) Baseline fluorescence and spontaneous neuronal activity (area under the curve (AUC)/min) during QW. (E) MLIN baseline fluorescence, (F) MLIN neuronal activity (WT 1,386, *Sca1* 714), (G) GoI baseline fluorescence and (H) neuronal activity (WT 114, *Sca1* 48), and (I) PN baseline fluorescence and (J) spontaneous neuronal activity (WT 112, *Sca1* 132).

(K) Heatmap depicting average neuronal activity in response to running onset for all MLINs in WT (left, blue frame) and *Sca1* mice (right, red frame).

(L and M) (L) Same as in (K) for GoI and (M) for PN.

(N–S) (N) Average population activity as function of instantaneous running velocity in MLINs (superimposed by sigmoidal fit), (O) fraction running-responsive MLINs per FOV (WT: 16 FOV [8 mice], *Sca1*: 9 FOV [6 mice]), (P) as in (N) for GoI, (Q) as in (O) for GoI (WT: 16 FOV [8 mice], *Sca1*: 6 FOV [4 mice]), (R) as in (N) for PN, (S) as in (O) for PN (WT: 14 FOV [8 mice], *Sca1*: 9 FOV [6 mice]). Data in (N), (P), and (R) mean ± SEM. Data presented as box plots throughout the manuscript display the median and interquartile range and whiskers extend to the minimum and maximum, unless differently stated. Scale bars, (B) 1 mm, (C) 100 μm, *p < 0.05, **p < 0.01, ***p < 0.001. (ML, molecular layer; PNL, Purkinje neuron layer; GCL, granule cell layer). Statistical test description and F/t/R values are in STAR Methods. See also Figures S1–S4.

but a decrease in GoI activity (Figure S2I) and no change in spontaneous PN activity in P60 *Sca1* mice (Figure S2J). Despite lacking the temporal resolution to resolve the high instantaneous pacemaker firing activities of 40–60 Hz,[21] larger fluctuations in the PN fluorescence traces occur, likely caused by pauses in simple spike firing.[22] Those fluctuations, however, did not differ between wild-type (WT) and *Sca1* mice.

Because GCaMP only allows for an approximation of calcium levels, we performed experiments using the ratiometric calcium indicator Twitch2B,[23] (Figures S3A–S3C), enabling more accurate measurements of actual calcium concentrations independent of expression levels. This analysis confirmed the reduced resting calcium concentration of MLINs in anesthetized *SCA1* mice (Figure S3D), and also unraveled reduced levels in GoI, but not in PNs at this early symptomatic stage (Figures S3E and S3F). We assessed neuronal activity levels and again found increased activity in MLINs in *Sca1* (Figure S3G); however, we found unchanged GoI activity (Figure S3H) and a slight, yet significant, increase in PNs (Figure S3I). As in PNs, we may mainly detect fluctuations in the calcium signal due to pauses in firing and complex spikes. Consequently, reduced pacemaker activity (as described for PNs in *Sca1*[24]), potentially even appears as greater fluctuations in the fluorescent signal.

To probe for probable impairments of sensorimotor integration, we compared neuronal activity levels during fb with those in darkness, (Figure S4A) and observed a strong linear correlation. However, we found *Sca1* MLINs displayed a leftward shift in the ratio of fb/dark activity, indicating alterations in sensorimotor integration (Figure S4A). Conversely, we found GoI to be less active in *Sca1* mice during fb and darkness (Figure S4B), whereas *Sca1* PNs were slightly more active during fb (Figure S4C). We also probed sensorimotor integration by assessing neuronal responses to an air puff, driving sensory, arousal, and startle-response signals[25] (Figures S4D–S4F). We observed a significant increase in neuronal activity in mutant MLINs (Figure S4G), a decreased response in GoI (Figure S4H), and an increase in PNs (Figure S4I). Together, these data show that neuronal dysfunction in *Sca1* mice is based on a combination of altered spontaneous activity and differentially impaired responsiveness to sensorimotor signals. Importantly, the cell type showing the strongest change in *Sca1* mice are MLINs, displaying increased activity levels, arguing for MLINs being hyperexcitable already in early symptomatic *Sca1* mice.

Neuronal coding space is strongly reduced in *Sca1* mice

To gain insight into cerebellar network dysfunction in early symptomatic *Sca1* mice, we investigated neural network representations of behavioral states and their distinctiveness. Several neuronal populations in the cerebellar cortex encode various sensorimotor signals in a multidimensional manner.[25–27] We chose a principal-component analysis (PCA)-based approach to investigate the dimensionality of the population dynamics in behaving mice. We assembled an input matrix, consisting of 0-centered, *Z* scored ΔF/F traces of all cells identified in a given field of view (FOV) and aligned it with the recordings of running speed, whisking, pupil width, and applied air puffs (Figure 2A). Analyses of the variance explained of the population activity revealed a multidimensional nature (Figure 2B). The first component (PC1) alone explained ~50% of the variance of the population activity in WT and *Sca1* (Figure 2C), dominated by locomotion and whisking. However, in *Sca1* mice, the variance of PC1 explained by locomotion, air puff, and whisking was reduced compared with WT (Figure 2D). Cell-type-specific regression analyses of PC1 revealed a significant reduction of the behavioral parameters for MLINs only, whereas for GoI it was mainly the contribution of the air-puff-representation that was affected (Figure 2D). In PNs, no significant difference in the encoding of behavioral parameters was found (Figure 2D). We also assessed the information content captured in PC2, which still contributed ~16% to the overall variance of the population activity (WT: 15.95% ± 4%, *Sca1*: 8.44% ± 2.6% of the variance). PC2 was also driven by locomotion as a single parameter but mainly captured all parameters combined, thus, the difference between active and quiescent phases (Figure S5). In contrast to PC1, we could not detect any differences in the variance explained by the individual behavioral parameters between WT and *Sca1* mice (Figure S5).

Neuronal activity patterns were multi-dimensional, consisting of at least 10 components. We thus asked how the geometry of these neuronal representations might be affected in *Sca1* mice. We computed the manifolds by projecting the multi-dimensional neuronal population activity to low-dimensional space, consisting of the first three components.[27–29] In WT mice, two distinct structures emerged, separating QW from locomotion (Figure 2E), corroborating previous reports.[27] Notably, the PC space representing QW was reduced in *Sca1* mice (Figure 2F), and the two subspaces were less segregated, as illustrated by the decreased Euclidean distance (Figure 2F). Together these data highlight a compromised encoding capacity of the cerebellar circuit in early symptomatic *Sca1* mice, an effect primarily driven by MLIN dysfunction.

To assess whether these deviations in neuronal function persist throughout the disease course, we performed similar experiments in P200 *Sca1* mice (Figures S6A and S6B). Under anesthesia, we observed a small but significant decrease in baseline fluorescence in MLINs (Figure S6C), no change in GoI (Figure S6D), and a pronounced increase in baseline fluorescence in PNs (Figure S6E), indicating a severe increase in cytoplasmic calcium levels in PNs at late disease stages. Neuronal activity of MLINs under anesthesia was still significantly increased (Figure S6F), which was also true for GoI (Figure S6G), whereas in PNs, we found reduced calcium fluctuations (Figure S6H). These findings were in line with the increased MLIN activity seen in awake mice during QW (Figure S6I). However, in awake mice, we still observed a decrease in GoI activity (Figure S6J), which could reflect the higher inhibitory tone during wakefulness, i.e., abolished under anesthesia, thereby potentially unmasking changes in intrinsic excitability. In PNs, we again observed decreased calcium fluctuations (Figure S6K). We quantified the response to locomotion and found a strong hyperresponsiveness of MLINs to running (Figure S6L), a hyporesponsiveness in GoI (Figure S6M), and a non-significant trend toward compromised locomotion responses in PNs (Figure S6N). Altogether, these data reveal that the observed hyperexcitability of MLINs remains conserved throughout the disease course in *Sca1* mice.

Given previous reports indicating hyperexcitability in PN dendrites as a critical contributor to PN degeneration,[30] we

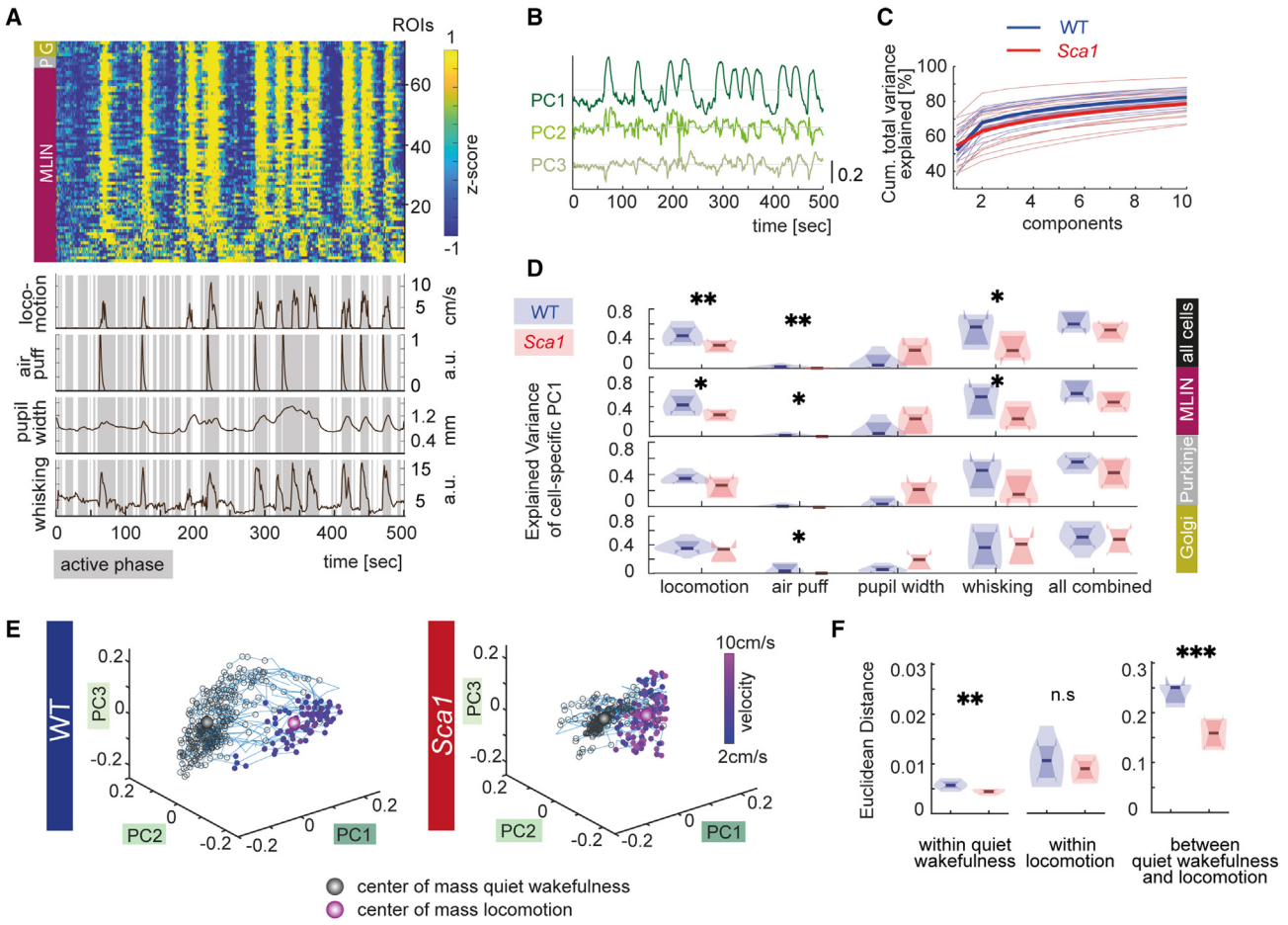

Figure 2. Compromised coding space of behavioral parameters in cerebellar cortex of *Sca1* mice

(A) Exemplary input matrix consisting of 0-centered and *Z* scored ΔF/F traces used for dimensionality reduction derived from all cells in one FOV of a feedback session of a WT mouse aligned with behavioral parameters (lower traces, magenta, MLIN; gray, PN; yellow, GoI).

(B) PC1, PC2, and PC3 time-series derived from input matrix shown in (A).

(C) Variance explained of the neuronal activity as a function of number of principal components in WT (blue, thin lines, individual FOV; thick line, mean) and *Sca1* mice (red). PC1 explains ∼50% of the variance in both WT and *Sca1* (WT 51.9% ± 8.6%, 16 FOV, 8 mice; *Sca1* 54.63% ± 11.6%, 14 FOV, 7 mice).

(D) Variance of PC1 (derived from all cells in a FOV or individual cell types), explained by the respective behavioral parameters in WT and *Sca1*.

(E) Representative manifold of QW and active states (as function of locomotion speed, color-coded) for WT and *Sca1* mice.

(F) Euclidean distance in PC space within and across brain states (WT: 12 FOV, 8 mice, *Sca1*: 10 FOV, 5 mice). Data in (D) and (E) are median + interquartile range. *p < 0.05, **p < 0.01, ***p < 0.001. See also Figures S5–S7.

assessed PN dendritic calcium signals, likely reflecting complex spiking[31] (Figures S7A and S7B). At P60, when no change in PN somata was observed yet, we already found evidence for increased dendritic excitability, seen in a higher fraction of active dendrites (i.e., dendrites displaying at least one clear calcium transient, Figure S7C), and an increase in dendritic calcium signals in *Sca1* mice (Figures S7D and S7E). These changes persisted until late disease stages (P200), with more active dendrites (Figure S7F) and higher activity levels (Figures S7G and S7H).

Mutant MLINs exhibit early connectivity and functional changes in *Sca1* mice

We sought to gain insight into the mechanisms governing early MLIN hyperexcitability in *SCA1*. By P30 cerebellar cortex is matured; therefore, we evaluated the expression of the calcium-binding protein parvalbumin (PV), a well-established MLIN marker, at P30, when *Sca1* mice lack motor incoordination (Figure S8A). Additionally, PV-expression levels are an indicator of neuronal activity, coinciding with plasticity-related learning processes.[32,33] Although the majority of P30, WT MLINs expressed medium levels of PV, 32% of MLINs presented high levels of PV in *Sca1*. The fraction of mutant MLINs expressing high levels of PV increased as a function of disease progression with 49% at P90 and 60% at P200 (Figure 3A). To exclude that the observed increase in mutant MLIN numbers, displaying high levels of PV was due to MLIN degeneration, we quantified the number of MLINs. Notably, until the end-stage, mutant MLIN numbers remained unchanged, suggesting that the early, yet gradual, increase in PV levels, reflect changes in MLIN

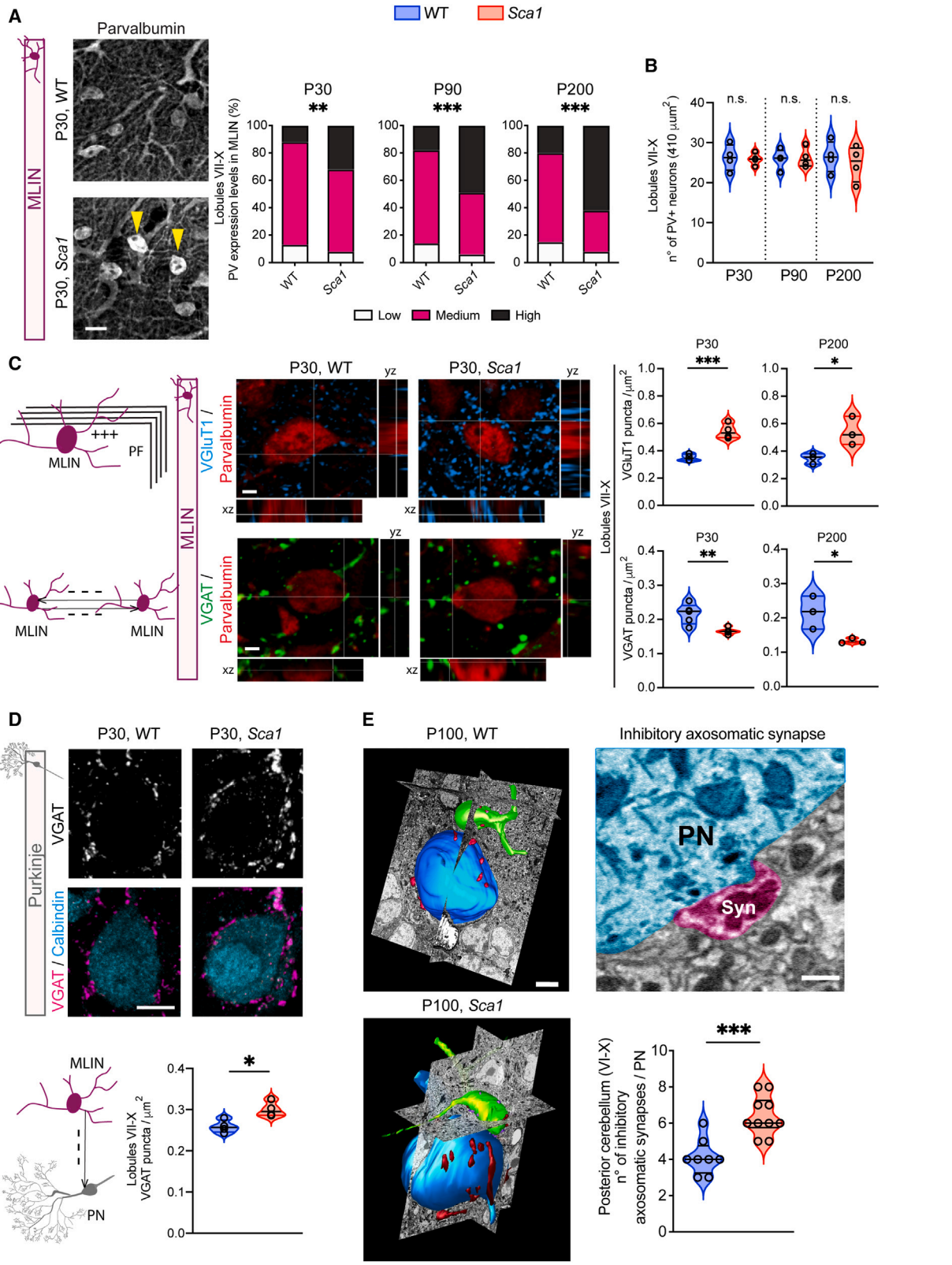

(legend on next page)

activity (Figure 3B). Furthermore, we examined PV levels in interneurons located in the primary motor cortex, a region involved in movement execution. No change in PV-expression levels or numbers was observed in *Sca1* (Figures S8B and S8C), suggesting that alterations in PV-expression levels were restricted to the cerebellum.

Next, we assessed the distribution of synaptic inputs onto MLINs and found that *Sca1* MLINs displayed increased numbers of excitatory synapses, marked by the vesicular glutamate transporter 1 (VGluT1) (Figure 3C). Concomitantly, mutant MLINs received fewer vesicular GABA transporter (VGAT)-positive homotypic inhibitory inputs from adjacent interneurons (Figure 3C). Both alterations in E/I inputs onto MLINs persisted until late disease stage. Because altered E/I connectivity on MLINs might influence PN responses, we examined the connectivity between MLINs and PNs at P30 and found an increased number of VGAT-positive inhibitory synapses surrounding PN somata in *Sca1* (Figure 3D). However, an increased number of inhibitory synapses on mutant PNs might reflect a delay in circuit refinement and maturation, with no consequences on PN function. Consequently, we evaluated the MLIN-PN connectivity via serial block-face scanning electron microscopy (SBF-SEM) in symptomatic mice. The 3D reconstruction of individual MLINs and their synaptic contacts onto PN somata revealed a significantly elevated number of axosomatic synapses in *Sca1*. This observation supports the notion that enhanced inhibitory connectivity between MLINs and PNs is related to higher MLIN activity levels, and this altered connectivity is maintained throughout disease (Figure 3E). Overall, these results demonstrate that in *Sca1* mice cerebellar dysfunction is based on the disinhibition of the cerebellar output, likely instigated by hyperexcitable MLINs, and that those deficits arise presymptomatically.

MLIN-mediated inhibition modulates SCA1 pathology

To probe for a causal role of MLIN hyperactivity in influencing motor pathology, we performed chemogenetic experiments. To selectively target MLINs, *Sca1* mice were crossed with homozygous *PV-Cre* mice to generate *Sca1::PV* or WT*::PV* animals (Figure 4A). To infect MLINs and not PNs, we injected the three common AAV serotypes: AAV2/1-hSyn-DIO-mCherry, AAV2/2-hSyn-DIO-mCherry, and AAV2/8-hSyn-DIO-mCherry into the adult WT*::PV* cerebellum. mCherry immunolabeling revealed that, although all serotypes primarily transduced MLINs, AAV2/8 infected a very high proportion of MLINs (Figure S9A). To characterize AAV2/8 serotype selectivity for MLINs, we performed intracerebroventricular (i.c.v.) injections in WT*::PV* neonates and analyzed the cerebellum at P35. mCherry immunolabeling highlighted several neuronal populations, with transduction being the highest in PNs, followed by granule cell layer (GCL) neurons and, lastly, MLINs, suggesting a developmentally regulated expression of the Cre-driver[34] (Figure S9B). To validate the specificity of AAV2/8-mediated transduction, AAV2/8-hSyn-DIO-mCherry or AAV2/8-hSyn-DIO-hM4D(Gi)-mCherry (inhibitory designer receptors exclusively activated by designer drugs [DREADD]) were injected into adult WT*::PV* cerebellum. Analysis of the transduced area revealed widespread mCherry expression, albeit restricted to MLIN somata and their perisomatic synapses onto PNs extending to the axonal initial segment, forming the pinceau (Figure S9C). Next, we injected AAV2/2-hSyn-DIO-hM4D(Gi)-mCherry and AAV2/8-hSyn-DIO-hM4D(Gi)-mCherry into WT*::Pcp2* neonates, wherein *Cre*-dependent expression is solely in PNs. AAV2/2 led to extensive mCherry expression in PNs throughout the cerebellum (~82.4%); however, AAV2/8 transduction was markedly lower in PNs (~42.4%) and exclusively within lobules IX and X (Figure S9D). In parallel, injections into the adult WT*::Pcp2* cerebellum (lobules VI and VII) revealed very high percentages of AAV2/2-mediated mCherry expression within adult PNs (~71.25%), but AAV2/8-mediated mCherry expression was present only within ~19.75% of PNs, suggesting that the floxed version of AAV2/8 serotype preferentially transduces adult MLINs (Figure S9D, lower graph). Lastly, quantification of the mCherry expression in 17 animals from our experimental cohort confirmed that AAV2/8 serotype transduces adult MLINs with a very high selectivity (~98% of all mCherry-positive cells), (Figure S9E).

To reduce the inhibitory tone onto PNs, we injected AAV2/8-hSyn-DIO-hM4D(Gi)-mCherry, bilaterally into the posterior cerebellum of P70, *Sca1::PV*, and WT*::PV* animals (Figure 4A). Expressed receptors were activated using the ligand clozapine-N-oxide (CNO) for three consecutive days, thereby suppressing synaptic transmission from MLINs onto PNs. CNO treatment, but not saline application, led to reduced PV-expression within MLINs, the reduction being stronger in *Sca1::PV* MLINs, suggesting that higher PV-expression in MLINs is dynamic and reversible (Figure 4B). Notably, diminished MLIN activity counteracted Calbindin reduction in *Sca1* PNs (Figure S10A), a disease-specific marker for PN dysfunction.[35] Moreover, restoration of phosphorylated CaMKII (P-CAMKII) expression within mutant PNs was observed, indicative of ameliorated intracellular calcium signaling and PN activation in response to reduced PN inhibition (Figure S10B).

We next assessed whether the improvement in disease-associated PN-specific hallmarks also affected symptomatic ataxia. To exclude side effects of CNO, we administered CNO (3 mg/kg) intraperitoneally (i.p.) to naive (WT) mice, 45 min before the

Figure 3. Altered inhibitory connectivity in the adult *Sca1* cerebellar cortex

(A) Representative confocal images (R.I.) of MLINs stained for parvalbumin (PV) from P30, WT, and *Sca1* cerebellum and quantitative analysis (Q.A.) of the percentage of neurons expressing low, medium, and high levels of PV at P30 (presymptomatic), P90 (symptomatic), and P200 (end-stage). Chi-squared test.

(B) No difference in MLIN numbers between WT and *Sca1* at different ages.

(C) R.I. of MLIN stained for PV, VGAT (inhibitory), or VGluT1 (excitatory) synaptic markers.

(D) R.I. of PNs stained for Calbindin and VGAT illustrating increased density of inhibitory synapses onto *Sca1* PNs soma.

(E) Representative 3D-SBF-SEM reconstructions of WT and *Sca1* PNs (blue), MLINs (green), inhibitory axosomatic synapses (red), excitatory synapses (magenta). Right: 2D-SBF-SEM image: inhibitory axosomatic synapse (magenta) and PN soma (cyan), showing elevated inhibitory axosomatic inputs onto mutant PNs. No. of animals: 3-6/genotype/age. Graphs (B–D) depict mean values/animal, (E) depicts mean value per PN. Scale bars, (A) 20, (C) 2, (D) 10, (E) 2 and 0.5 (μm). *$p < 0.05$, **$p < 0.01$, ***$p < 0.001$. See also Figure S8.

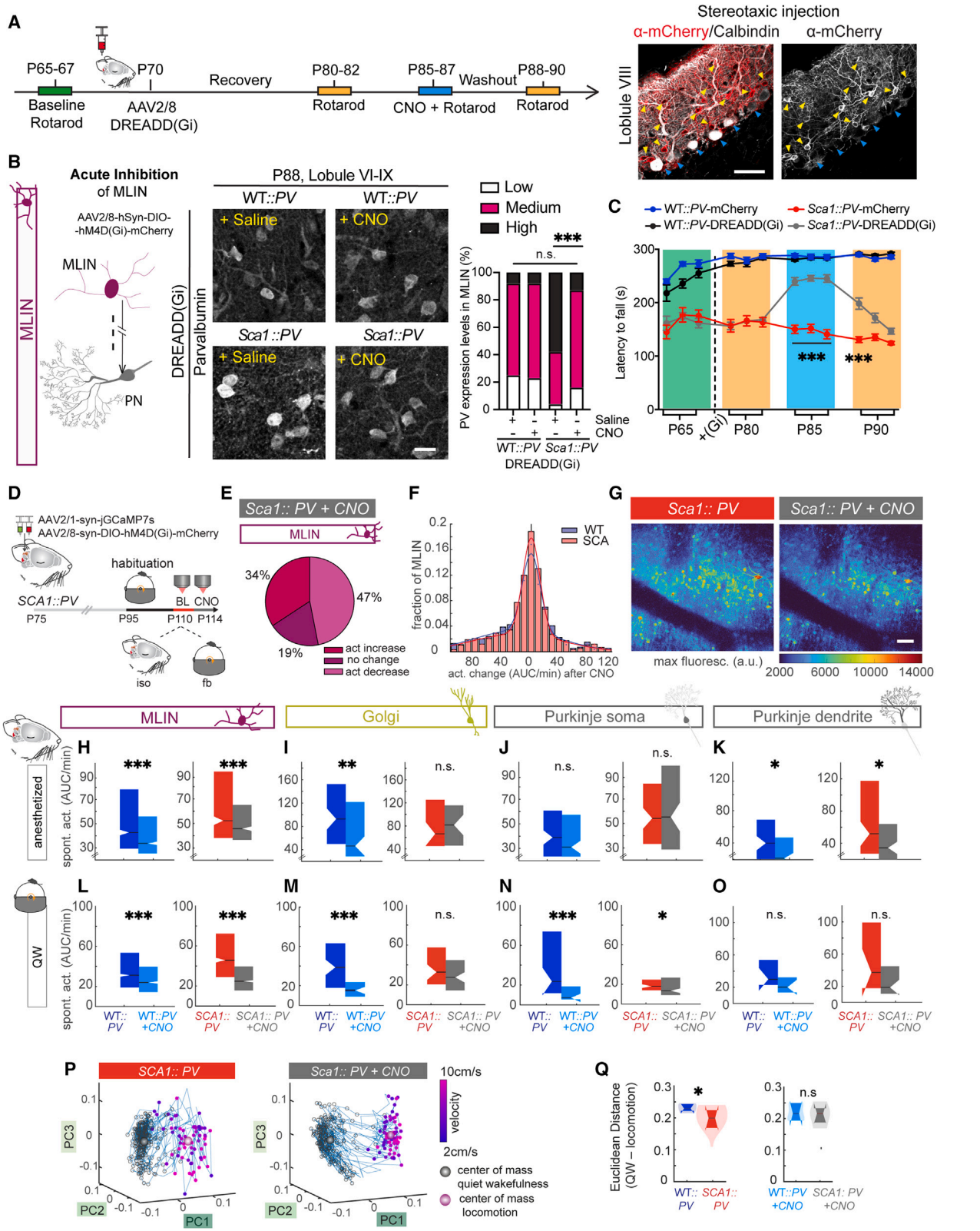

(legend on next page)

rotarod test, which did not cause any adverse effects (Figure S11A).[36] Subsequently, we tested the inhibitory DREADD-expressing mice for rotarod performance before and after the surgical procedure. At P85, mice were tested for three consecutive days on the rotarod after CNO/saline injection. Surprisingly, suppressing synaptic transmission between MLINs and PNs did not have any effect on WT::*PV* animals. However, a substantial improvement in motor performance was observed in *Sca1::PV* animals after CNO injections (Figure 4C). *Sca1::PV* mice displayed improved rotarod performance, even after 24 h of CNO washout, suggesting some form of lasting plasticity. To exclude that the amelioration in motor incoordination was due to non-specific viral transduction of brain stem and spinal cord neurons, we performed immunostaining for mCherry, whose expression remained localized within the cerebellum, with no unspecific spreading to other CNS regions (Figures S11B and S11C).

Additionally, we probed the impact of chemogenetic inhibition of MLINs on neuronal function. We co-injected AAV2/8-hSyn-DIO-hM4D(Gi)-mCherry and AAV2/1-syn-jGCaMP7s into P75, *Sca1::PV*, and WT::*PV* mice and performed *in vivo* calcium imaging in ∼P110 aged mice (Figure 4D). Although CNO application alone in control mice had no effect on neuronal activity (Figures S11D–S11I), we found that ∼50% of MLINs in DREADD-expressing mice displayed reduced neuronal activity under light anesthesia. About 20% of MLINs did not overtly change their activity levels, and the remaining MLINs increased their activity (Figure 4E). The overall distribution of absolute activity changes upon CNO shows a reduction of activity levels in a substantial proportion of MLINs (Figures 4F–4H). We observed reduced activity in GoI exclusively in WT::*PV* mice (Figure 4I), whereas calcium signals in PNs somata were not affected by the CNO-triggered silencing of MLINs (Figure 4J). However, a significant decline in calcium signals in PN dendrites in WT::*PV* and *Sca1::PV* mice was observed (Figure 4K). These findings were corroborated by recordings in awake mice, in which CNO administration revealed a strong reduction in the spontaneous activity of MLINs during QW (Figure 4L). In awake mice, GoI activity decreased upon CNO in WT::*PV* and as a trend in *Sca1::PV* mice (Figure 4M), as did the calcium signal fluctuations in PN somata (Figure 4N), potentially reflecting a more stable pacemaker firing activity, which would cause less fluctuations in the fluorescence trace. PN dendrites were not affected upon CNO in awake mice (Figure 4O). We examined whether the compromised coding capacity would normalize upon chemogenetic dampening of MLIN excitability. Computing the manifolds of all neurons in a given FOV, we found two subspaces (Figure 4P), which were less discrete in *Sca1::PV* mice. Intriguingly, after CNO application, the subspaces became more discrete, and the Euclidean distance between both states became insignificant between WT::*PV* and *Sca1::PV* mice (Figure 4Q). The investigation of neuronal function upon MLIN silencing thus demonstrates a normalization not only of activity levels in *Sca1* but also of the networks' coding capacity.

Enhancing MLIN activity is sufficient to induce SCA1-like pathology in WT mice

We hypothesized that augmented inhibition could impair PN function, thereby inducing motor incoordination; thus, we mimicked the altered mutant MLIN activity in WT animals. We injected excitatory DREADDs (AAV2/8-hSyn-DIO-hM3D(Gq)-mCherry) in the WT::*PV* cerebellum (Figures 5A and 5B). Elevated PV-expression within WT::*PV* MLINs, similar to those in *Sca1::PV* MLINs, after CNO application was observed (Figure 5C). Importantly, we also found that the rotarod performance of WT::*PV* mice that received CNO injections drastically dropped, almost reaching levels observed in *Sca1::PV* mice (Figure 5D). Centered on the acute MLIN overactivation data and the fact that NDs show a progressive increase in symptoms, we mimicked this aspect by chronically activating MLINs either for 30 or 60 days in WT::*PV* mice (Figure 5E). Because SCA1 pathology is characterized by initial dysfunction in PN spines, detected by reduced Homer-3 expression,[14] we examined Homer-3 levels. Notably, 30 days of CNO application led to a significant reduction in Homer-3-positive puncta, which was maintained after 2 months of CNO treatment, suggesting a thresholding effect (Figure 5F). Moreover, P-CAMKII levels in PN soma

Figure 4. Acute MLIN activity reduction influences cerebellar network responses and alleviates motor deficits

(A) Experimental design showing acute MLIN inhibition in WT::*PV and SCA1::PV* mice via AAV2/8-DREADD(Gi). Right: R.I. of mCherry expression within WT::*PV* MLINs (yellow arrowheads), note the absence of mCherry staining in PNs (blue arrowheads).

(B) R.I. of comparable PV expression in WT::*PV and Sca1::PV*-expressing DREADD(Gi) MLINs after saline/CNO injection, n = 3 mice/group.

(C) Rotarod measurement reveals improved motor performance of *Sca1::PV*-DREADD(Gi)+CNO mice vs. saline group. WT::*PV*+saline n = 9; WT::*PV*+CNO n = 8; *Sca1*::*PV*+saline n = 8; *Sca1::PV*+CNO n = 10 mice.

(D) *In vivo* imaging experiment design. Same neurons were recorded (fb, iso) at baseline (BL, w/o CNO, P110) and upon CNO application.

(E) Fraction of neurons with increased, decreased, or no change in activity in *Sca1::PV* MLIN+CNO.

(F) Absolute activity changes in MLINs upon CNO.

(G) Maximum intensity projection of a *Sca1::PV* mouse before and after CNO.

(H–K) (H) MLIN activity under anesthesia before and after CNO in WT::*PV* (left, 1,088 MLINs) and in *Sca1::PV* (right, 548 MLINs), (I) same as in (H) for GoI in WT::*PV* (78 GoI) and *Sca1::PV* (38 GoI), (J) and in PN in WT::*PV* (102 PN) and *Sca1::PV* (83 PN) and (K) calcium signals in PN dendrites in WT::*PV* (83 PN dendrites) and *Sca1::PV* (88 PN dendrites), data in (H)–(K) from WT::*PV*: 12 FOV, and *Sca1::PV*: 8 FOV, 5 mice/genotype).

(L–O) (L) QW spontaneous activity of MLINs before and after CNO in WT::*PV* (1,316 MLINs) and *Sca1::PV* (813 MLINs), (M) of GoI in WT::*PV* (82 GoI) and *Sca1::PV* (56 GoI), (N) of PN in WT::*PV* (49 PN) and *Sca1::PV* (76 PN) and (O) calcium signals in PN dendrites in WT::*PV* (12 PN dendrites) and *Sca1::PV* (19 PN dendrites), data from WT::*PV*: 17 FOV, and *Sca1::PV*: 17 FOV, 7 mice/genotype).

(P) Example manifold of all neurons in a FOV from a *Sca1::PV* mouse, depicting less discrete segregation of QW and active states (running speed color-coded), which is improved after CNO application (right).

(Q) Euclidean distance in PC-space between the center of mass of QW and locomotion (before CNO: WT::*PV*: 10 FOV, *Sca1::PV*: 12 FOV, after CNO: WT::*PV*: 9 FOV, *Sca1::PV* 11 FOV, (5–6 mice/genotype). Graph (C) represents mean ± SEM, data in (H–O) and (Q) represent median and interquartile range. Scale bars, (A) 100, (B) 20, (G) 50 (μm). *p < 0.05, **p < 0.01, ***p<0.001. See also Figures S9–S11.

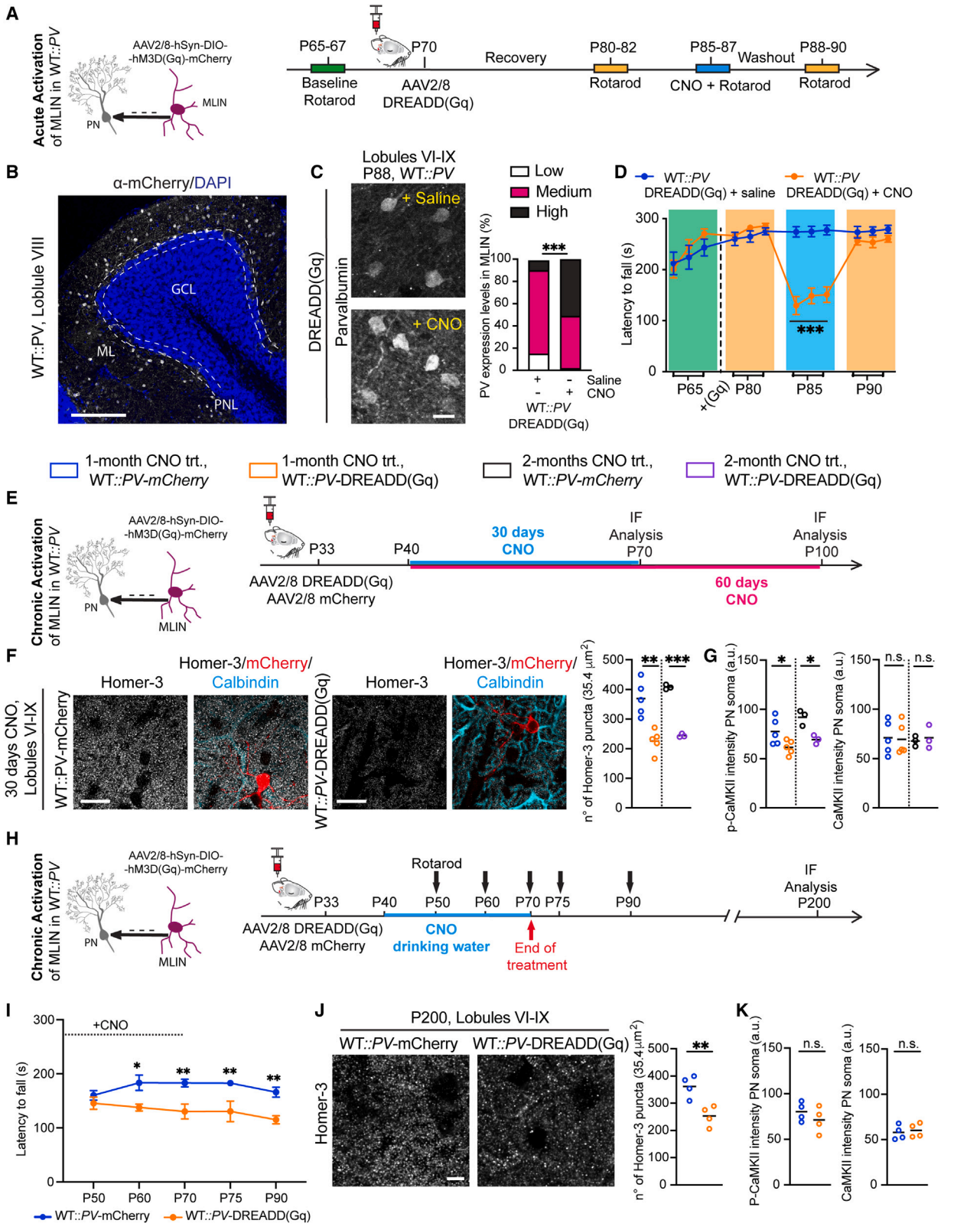

(legend on next page)

were significantly reduced to levels observed in *Sca1* PNs (Figure 5G). Subsequently, we examined whether the cellular changes translated into motor dysfunction (Figure 5H). Rotarod measurements during chronic CNO application revealed a consistent decline in the latency to fall in WT*::PV* mice (Figure 5I). Interestingly, motor incoordination was maintained at least until 20 days after halting CNO treatment, suggesting that chronic MLIN overactivation, even in WT*::PV* mice, not only induces a SCA1-like phenotype but also leaves a long-lasting trace (Figure 5I). Lastly, we analyzed the same cohort of mice 130 days after halting CNO treatment and found that Homer-3-expression remained reduced (Figure 5J), whereas P-CAMKII levels were somewhat normalized within PN soma of WT*::PV* mice (Figure 5K). These results show that MLIN-mediated, elevated inhibition of PNs, non-cell autonomously, promotes cellular pathology within PNs and triggers manifestations of ataxia-like symptoms in WT*::PV* mice, lacking disease-causing mutations.

Chronic disinhibition of PNs is neuroprotective in *Sca1* mice

Next, we hypothesized that 30 days of chronic reduction in MLIN activity in *Sca1::PV* mice should provide long-term amelioration in cerebellar dysfunctions. To this end, we selectively expressed inhibitory DREADDs in WT*::PV* and *Sca1::PV* MLINs at P40, followed by the chronic administration of CNO in drinking water (40 μg/mL) for 30 days. Analysis performed after stopping the CNO treatment, at an age corresponding to the late disease stage (Figure 6A), revealed sustained reduction of PV-expression, specifically within mutant MLINs (Figure 6B), and normalized P-CAMKII levels, with no changes in total CAMKII levels (Figure 6C, S12A, and S12B). Moreover, a beneficial effect on PN synaptic structures was observed via an increase in Homer-3 immunoreactive puncta at P180, suggesting that the amelioration in pathology due to reduced MLIN activity is maintained long term, despite halting CNO-mediated modulation (Figure 6D). This overall protective effect was also reflected by sustained PN numbers (Figure 6E), indicating that reduced inhibitory drive onto *Sca1* PNs ameliorates cerebellar degeneration. Next, we assessed whether MLIN modulation can alter the activation of astrocytes and microglia, which is observed early in SCA1 pathogenesis.[37] Gliosis levels were significantly lower in cerebellar lobules where MLIN activity was reduced in comparison with neighboring non-transduced lobules, indicating a general beneficial effect of reducing MLIN activity in *Sca1* mice (Figure S12C). Because PN dendrites exhibited hyperactivity, we examined whether reducing PN activity would be neuroprotective. Inhibitory DREADD AAV2/2-hM4D(Gi)-mCherry was expressed in WT*::Pcp2* and *Sca1::Pcp2* mice (Figure S12D). Acute CNO application reduced P-CAMKII expression in both WT and *Sca1* PNs, confirming reduced intracellular calcium-signaling and PN activity (Figure S12E). Chronic CNO treatment from P60-P70, surprisingly, anticipated PN degeneration selectively in *Sca1* mice (Figures S12F and S12G). This differential outcome on disease pathology dependent on the neuronal population targeted, highlights the contribution of MLIN hyperresponsiveness to SCA1 pathology.

Lastly, measurement of rotarod performance, during and after CNO application, revealed a striking amelioration of motor coordination deficits in *Sca1::PV* animals, expressing inhibitory DREADD in MLINs (Figure 6F). Notably, despite the termination of the CNO application at P90, *Sca1::PV* symptomatic animals displayed a significantly improved motor performance compared with the untreated *Sca1::PV* group for another 2 months, whereas no significant effect on WT*::PV* motor performance was observed (Figure 6F). Chronic CNO application delayed the onset of the hindlimb clasping phenotype, a measurement that directly correlates with disease severity, with higher scores indicative of symptom worsening (Figure 6G).

Proteomic analyses of adult MLIN identifies widespread synaptic alterations

Because functional MLIN alterations in SCA1 are strong contributors to the degenerative process, we investigated the molecular signature, accounting for the functional changes in mutant MLINs. We undertook a FACS approach to selectively isolate adult PV-positive MLIN for proteomic analysis (Figure 7A).[38] MLINs were labeled by injecting AAV8- hSyn-DIO-mCherry into P30-35 WT*::PV* and *Sca1::PV* animals. Two weeks post surgery, cerebellar tissue was dissociated, and viable single neurons were sorted for mCherry and Hoechst (Figure S13A). We confirmed that the sorted neurons were viable PV-positive interneurons by culturing them for 24 h and staining for MLIN marker PV (Figure S13B). Sorted MLINs were lyophilized and processed for mass spectrometry, revealing that the sorted neurons present typical MLIN markers (Figure 7B). Proteomic analyses highlighted a large number of downregulated proteins in *Sca1* MLINs (Figure 7C; Table S1). Panther (protein analysis through evolutionary relationships) protein class analyses of downregulated proteins revealed that 34.2% of those belong to the metabolite interconversion enzyme class, 17.8% to RNA metabolism protein, 11% to transporter protein class, and 9.6% to membrane trafficking proteins (Figure 7D). As previously shown,

Figure 5. Mimicking mutant MLIN hyperresponsiveness in WT*::PV* mice

(A) Experimental design for acute cerebellar MLIN activation in WT*::PV* mice.
(B) R.I. of mCherry expression in WT*::PV*, lobule VIII.
(C) Mimicking mutant MLIN hyperresponsiveness in WT*::PV* MLINs by CNO stimulation of excitatory DREADD (Gq), increases PV levels.
(D) WT*::PV* animals display impaired motor performance on rotarod vs. saline group after CNO injection WT*::PV*+saline n = 7, WT*::PV*+CNO n = 10 mice).
(E) Experimental design for chronic MLIN activation in WT*::PV* animals.
(F) R.I. and Q.A. of reduced Homer-3 expression in WT*::PV*-mCherry and WT*::PV*-DREADD(Gq) mice after 30 or 60 days of CNO treatment.
(G) Q.A. of reduced P-CAMKII expression in WT*::PV*-DREADD(Gq) and WT::*PV*-mCherry PNs, no change in total CAMKII.
(H) Experimental design for chronic WT::*PV* MLIN activation, analyzed at P200 (bold arrow: longitudinal rotarod measurement throughout).
(I) Chronic CNO administration impairs motor performance in WT::*PV*-DREADD(Gq) mice, n = 8 animals/group.
(J) R.I. and Q.A showing reduced Homer-3 expression in WT::*PV*-DREADD(Gq) vs. WT::*PV*-mCherry.
(K) Q.A. of P-CAMKII and CAMKII expression after chronic activation of MLINs in WT*::PV* mice. n = 3–5 mice/analysis. Graphs (D and I) represent mean ± SEM, (F, G, J, and K) depict mean values/animal. *p < 0.05, **p < 0.01, ***p < 0.001. Scale bars, (B) 200, (C) 10, (F) 10, (J) 10 (μm).

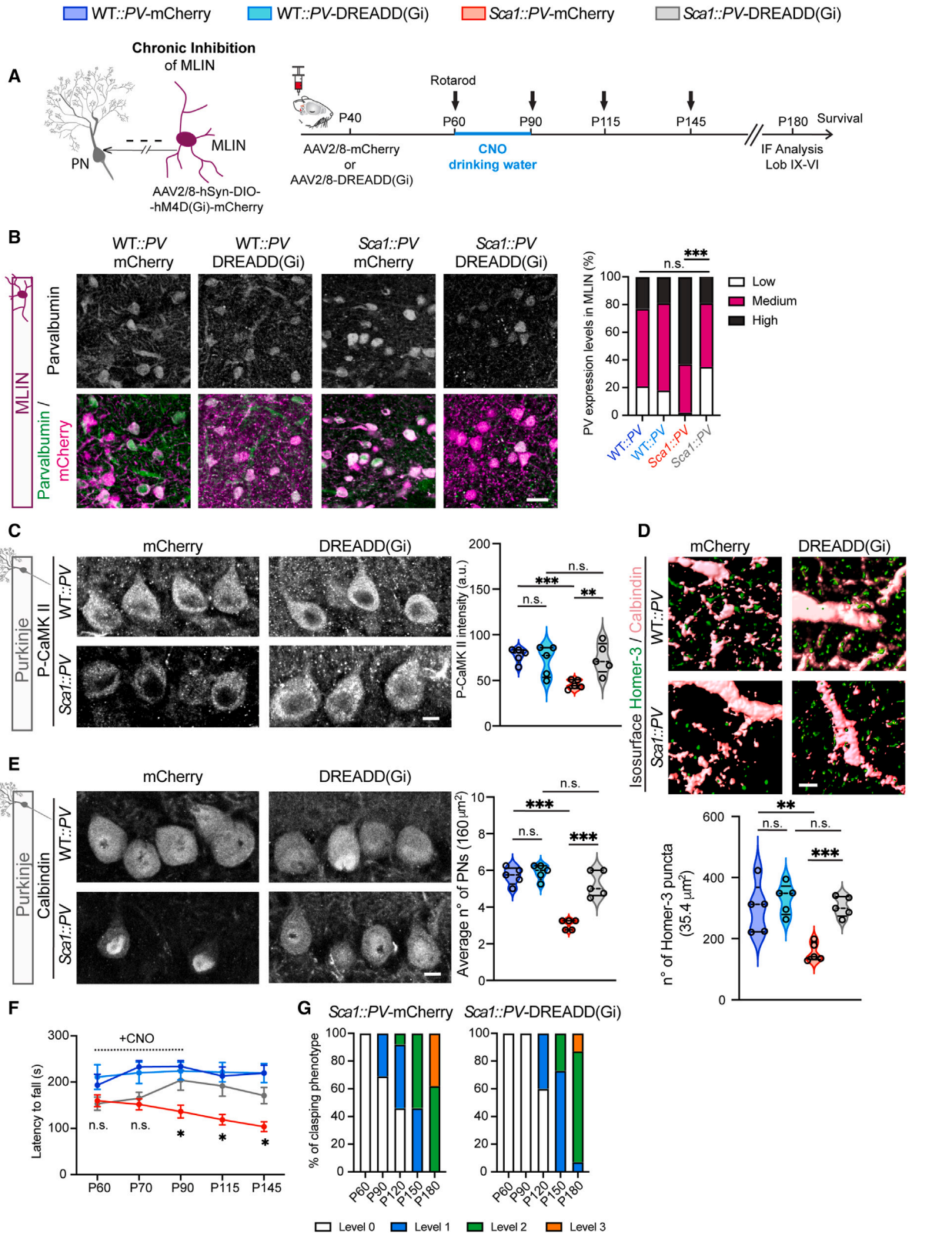

(legend on next page)

proteins involved in synaptic function are prominently altered in *Sca1* PNs.[14] Similarly, MLINs presented an altered synaptic profile, with proteins involved in synaptic transmission being shared and reduced in expression in both MLINs and PNs, indicating that mutant Ataxin-1 selectively affects the expression of synaptic proteins of dedicated cerebellar circuit elements (Figures 7D and S13C).

Panther protein class analysis of the upregulated proteins revealed that 17.2% of those proteins belong to the metabolite interconversion enzyme group, 11.1% to protein modifying enzyme and 9.1% to transporter protein class (Figures 7E and 7F). Interestingly, we identified the increased expression of the α-amino-3-hydroxyl-5-methyl-4-isoxazole-propionate (AMPA) receptor-associated protein, ferric chelate reductase 1-like (Frrs1l), involved in AMPA receptor biogenesis and trafficking.[39] Immunoblotting total cerebellar lysates displayed no difference in Frrs1l expression in *Sca1* (Figure S13D). However, immunostaining MLINs against Frrs1l revealed the elevated expression of Frrs1l in *Sca1* MLINs. As further evidence, higher Frrs1l levels positively correlated with increased PV levels in *Sca1* MLINs within the posterior cerebellum (Figure 7G). Notably, Frss1l levels exhibited an anterior-posterior gradient, akin to that observed in the degeneration of PNs. A higher fraction of posterior MLINs, expressing elevated levels of Frrs1l at both symptomatic (P100) and late symptomatic (P200) stages, was observed (Figure 7H). Consequently, we assessed AMPA receptor-subunit, GluR2 expression in MLINs, which revealed a dramatic increase in GluR2 immunoreactivity on the surface of *Sca1* MLINs (Figure 7I), likely accounting for the increase in MLIN excitability.

Conserved hyperresponsiveness of human *SCA1* patient iPSC-derived GABAergic neurons

To validate our findings in the context of human pathology, we generated induced GABAergic neurons (iGNs) from induced pluripotent stem cells (iPSCs)[38] derived from three *SCA1* patients and their unaffected siblings (Figure S14A). We evaluated the purity of our cultures and performed an in-depth characterization of the generated interneuron populations (Figure S14B). Two-week-old iGNs were 91% positive for the neuronal marker MAP2 and negative for astrocyte marker GFAP (Figures S14B and S14C). Of the 91% MAP2-expressing neurons, 91% expressed the neurotransmitter GABA (Figure S14D). Of the 91% GABA-positive neurons, 93% were PV-positive, but lacked Calbindin and expressed Kv1.2, indicating that neurons were excitable and active (Figures S14E and S14F). Because our protocol generated pan-inhibitory interneurons, we immunostained for SORCS3, an MLIN-specific marker, which is absent in cerebellar GoI, PNs, and cortical interneurons.[40] A fraction of PV-positive iGNs expressed high levels of SORCS3 (62%), suggesting that at least a fraction of iGNs also possess MLIN-like characteristics (Figure S14G).

Subsequently, immunostaining revealed higher immunoreactivity for FRRS1l and GluR2 within human *SCA1* iGNs compared with *Controls* (*CNTRLS*) (Figure 8A). The higher expression of FRRS1L in *SCA1* iGNs directly correlated with elevated PV immunolabeling, ∼57% of iGNs displayed elevated PV levels (Figure 8B). These results corroborate findings in *Sca1* mice in Figure 3A, in which ∼49% of P90, MLINs exhibited high PV expression. Because *in vivo* mutant MLINs are excessively hyperexcitable and hyperresponsive to sensorimotor stimuli, we wondered whether this hyperexcitability of MLINs is a conserved feature, detectable in *SCA1* iGNs. Live-cell calcium imaging was performed on human iGNs that were transduced with the green calcium indicator AAV2/1-hSyn-GCaMP6s, 5-days post differentiation, and calcium imaging was conducted at day *in vitro* (DIV)12 (Figure 8C). Both *CNTRL* and *SCA1* iGNs fell into two differentially responding populations. Among the neurons that increased their cytoplasmic calcium levels after 50 mM KCl stimulations, two populations of MLINs were observed, labeled as high and low-responding iGNs (Figure 8D). Notably, a substantial proportion, ∼78% of *SCA1* iGNs, fell into the high-responding category (median $\Delta F < 1.5$ at 70 s), displaying prominently higher calcium signals compared with the *CNTRL* iGNs, where only 58% of the iGNs fell into the high-responding category. Moreover, the amplitude in high-responding MLINs at 70 s was higher in *SCA1* iGNs compared with *CNTRL* iGNs (Figure 8D, middle panel). Mutant iGNs exhibited a significantly longer rise time in the high-responding population compared with healthy iGNs (Figure 8D, right panel).

The high expression levels of FRRS1L in *SCA1* iGNs indicated a probable link between FRRS1L levels and MLIN hyperresponsiveness. To clarify this association, lentivirus-mediated overexpression of FRRS1L (LV::*FRRS1L-myc*) or knockdown of FRRS1L (LV::*sh-FRRS1L-GFP*) was performed (Figures 8E and S15A). Calcium imaging revealed that FRRS1L-overexpressing *CNTRL* iGNs presented higher calcium signals, closely mimicking those observed in *SCA1* iGNs (Figure 8F). By contrast, the overexpression of FRRS1L in *SCA1* iGNs did not further elevate calcium traces, suggesting a ceiling effect (Figure S15B). *FRRS1L* knockdown was performed by LV carrying the small hairpin (sh) RNA-tagged to GFP; therefore, red calcium indicator AAV2/1-hSyn-RCaMP was used, and we first confirmed that both calcium indicators elicited similar responses (Figure S15C). The knockdown of *FRRS1L* dramatically reduced

Figure 6. Chronic suppression of MLIN activity delays SCA1 pathology

(A) Experimental design for chronic MLIN inhibition.

(B) R.I. of PV expression within WT::*PV* and *Sca1*::*PV* MLINs. Chronic inhibition of *Sca1*::*PV* MLINs via DREADD(Gi), normalizes PV expression to WT levels.

(C) R.I. and Q.A. of restored P-CAMKII expression in PNs.

(D) 3D-isosurface reconstructions showing elevated Homer-3 and Calbindin expression within the molecular layer in *Sca1*::PV-DREADD(Gi) mice.

(E) R.I. of Calbindin labeled PNs from four conditions and Q.A. of sustained PN numbers in *Sca1*::*PV-DREADD*(*Gi*) vs. *Sca1*::*PV*-mCherry group.

(F) CNO chronic administration delays appearance of motor symptoms in *Sca1*::PV-DREADD(Gi) mice, WT::*PV*-mCherry n = 13; WT::PV-DREADD(Gi) n = 11; *Sca1*::*PV*-mCherry n = 13; *Sca1*::PV-DREADD(Gi) n = 10 mice.

(G) Clasping phenotype across disease progression in *Sca1*::*PV*-mCherry and *Sca1*::PV-DREADD(Gi), showing reduced clasping severity in DREADD(Gi) cohort. Graphs (C–E) depict mean values/animal, (F) represents mean ± SEM. *$p < 0.05$, **$p < 0.01$, ***$p < 0.001$. Scale bars, (B) 20, (C and E) 20, (D) 4 (μm). See also Figure S12.

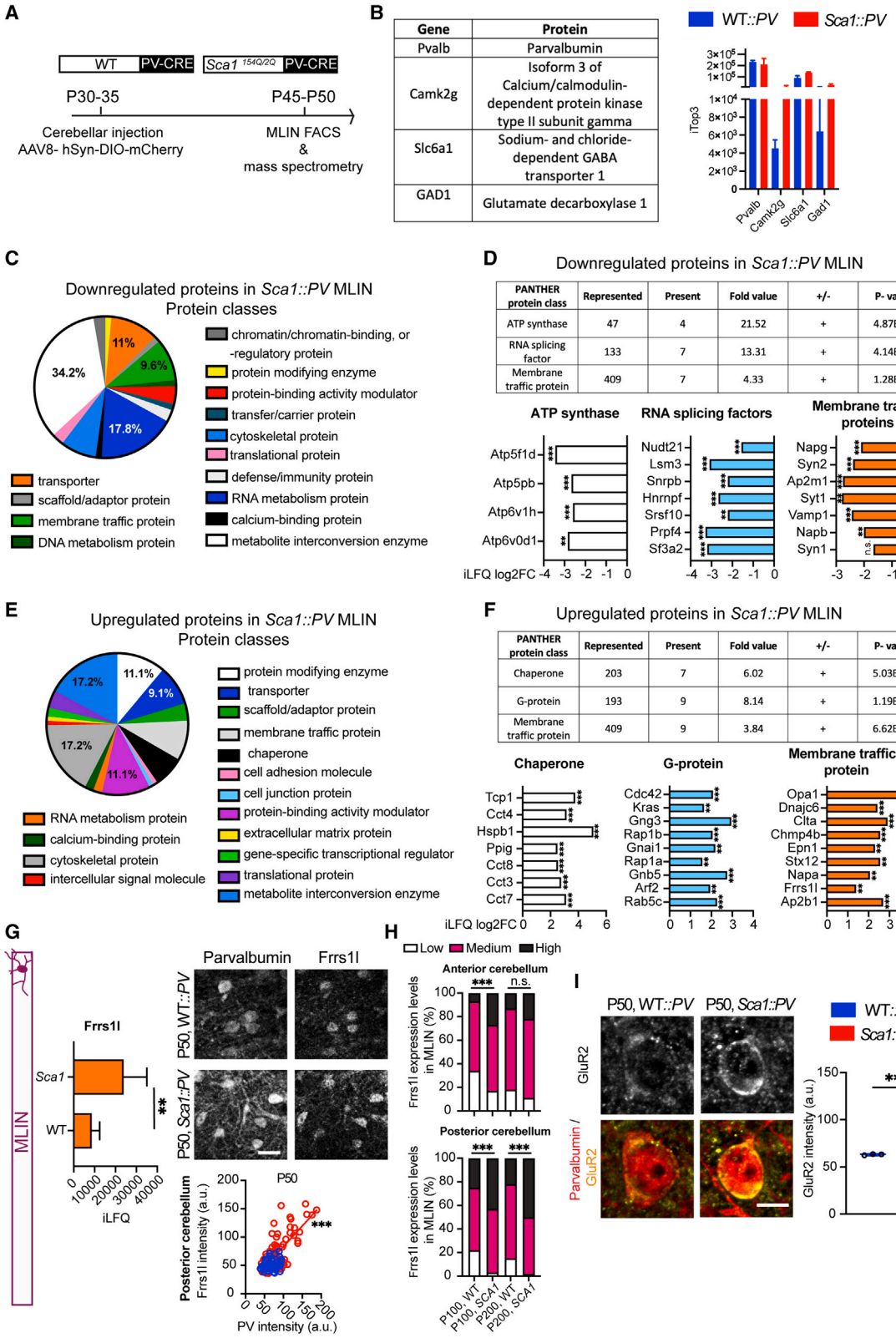

(legend on next page)

calcium responses in both *SCA1* and *CNTRL iGNS* (Figures 8G and S15D). Due to the very high transduction efficiency of LVs, FRRS1L overexpression completely abolished the low-responding population of iGNs, and *FRRS1L* knockdown completely abrogated the high-responding fraction of iGNs (Figure S15E), thus highlighting the role of FRRS1L in governing MLIN hyperresponsiveness in SCA1.

DISCUSSION

This study provides for the first-time direct evidence for a causal impact of a hitherto poorly recognized circuit element, namely MLINs, in the degenerative process of *Sca1* PNs. Our data demonstrate that hyperexcitability of MLINs occurs very early in the disease process and persists until the end-stage. Together with an enhanced synaptic connectivity between MLINs and PNs, it compromises cerebellar sensorimotor processing, fuels PN synaptic dysfunction, and causes motor deficits. Our data, using chemogenetic modulation of MLINs, demonstrate that circuit dysfunction is sufficient to trigger SCA1-disease-like alterations and that PNs remain the most vulnerable neurons within the cerebellum. We further identify the molecular signature of mutant MLINs, revealing that enhanced Frrs1L expression influences MLIN activity responses. This work provides crucial evidence for circuit dysfunction as an important driver of SCA1 pathophysiology, and neurons, which primarily don't degenerate, play a decisive role in shaping circuit output and triggering the pathology.

The cerebellum is a multimodal sensorimotor integration hub, facilitating the fine-tuning of movements, balance, stance, and cognition, all of which are compromised in SCAs.[41] Our *in vivo* calcium imaging experiments unexpectedly unraveled a selective sensorimotor hyperresponsiveness of MLINs, which provide the main inhibitory input onto PNs. MLINs receive excitatory sensorimotor signals through PFs and also from CFs via glutamate spillover.[17] Moreover, MLINs are reciprocally connected, enabling tightly regulated feedforward and fb inhibition. Recent studies describe a cardinal role for MLINs in valence coding, associative learning,[36] as well as licking-related activity, modified by, e.g., motivational state.[42,43] Chemogenetic-mediated MLIN inhibition reduces lick rate and precision, emphasizing the role of MLIN-mediated PN inhibition for movement control.[42] Notably, optogenetic stimulation of MLINs can trigger motor behavior[44] through PN inhibition, and concerted MLIN activity scales with locomotion speed, mediated by the silencing of PN.[31]

We show that the increase in spontaneous neuronal activity of MLINs in *Sca1* reduces the coding space and renders brain state representations less distinct, thus sending ambiguous signals to PNs. Notably, MLINs display irregular fast spiking, which is mainly regulated intrinsically.[17] Thus, the observed increase in spontaneous activity of MLINs during stationary/quiescent epochs could relate to increased intrinsic hyperexcitability and/or defective reciprocal inhibition due to reduced synaptic connections among MLINs. Although we found MLINs to be hyperexcitable, we observed a reduction in GoI sensorimotor responses. GoI are inhibitory GABAergic neurons, located within the GCL, providing crucial regulation and gain control of granule cell activity via lateral inhibition in a feedforward inhibitory loop.[25,45,46] Importantly, GoI receive inhibitory input from the MLINs, whereas both neuronal types are activated by PFs.[45,47] It is possible that the hyporesponsiveness of mutant GoI is a consequence of MLIN hyperactivity, which could potentially affect PF input, resulting in a vicious stimulation cycle.

Our data demonstrate that mutant MLINs exhibit aberrant spontaneous activity and aberrant responses to sensorimotor input, persisting from early until late disease stages. Together with higher synaptic connections onto PNs, we propose that PNs undergo a dual hit by MLINs, thus strongly disrupting correlated PN activity and compromising their pacemaker firing properties.[24] Additionally, we demonstrated dendritic hyperexcitability of PNs, present throughout the disease course, suggesting that increase in PN dendritic excitability might represent a homeostatic mechanism in response to excessive inhibition, resulting in a maladaptive process. Nonetheless, we did not observe major alterations in somatic calcium signals in PNs and found reduced spontaneous activity, along with a strong increase in cytosolic calcium levels in PNs somata at late disease stages. However, the very high instantaneous firing rates of PNs (20–70 Hz)[48] and the rather slow kinetics of calcium indicators, primarily facilitate the detection of simple spike pauses.[22] Hence, our approach falls short in detecting more subtle changes in PN activity.

Moreover, several studies highlight deficits in PNs, associated with genes regulating calcium homeostasis in different SCA mouse models, such as impaired transactivation of retinoic acid-related orphan receptor (ROR) alpha by mutant Ataxin-1.[49] Impaired calcium homeostasis is a convergent pathway in SCAs, involving voltage-gated calcium channels[50] such as SCA6, [51] SCA7[52], and mutations in the α-subunit of $Ca_v2.1$ channel, causing episodic forms of ataxia, such as EA2.[53,54] Furthermore, BK channels, involved in establishing PN pacemaker activity, are downregulated in SCA1 mice, and enhancing their expression restores PN pacemaker firing.[24] Intriguingly, a recent publication suggests a negative fb loop by which PN, in turn, inhibit MLINs;[55] thus, it is conceivable that compromised PN pacemaker firing could affect MLIN

Figure 7. Frrs1l likely determines MLIN hyperresponsiveness

(A) Experimental design for isolating mCherry labeled MLINs from adult WT::*PV* and *Sca1::PV* cerebellum (n = 9 mice/genotype).
(B) MLIN-selective markers identified via mass spectrometry (MS) from one experiment (3 cerebella/genotype).
(C) Downregulated (iLFQ Log2FC 1.4) proteins in *Sca1::PV* MLINs.
(D) PANTHER overrepresentation test: downregulated protein classes in *Sca1::PV* MLINs.
(E) Upregulated (iLFQ Log2FC 1.4) proteins in *Sca1::PV* MLINs.
(F) PANTHER overrepresentation test: upregulated protein classes in *Sca1::PV* MLINs.
(G) MS-based iLFQ values of Frrs1l. R.I. of increased Frrs1l and PV expression in MLINs from WT::*PV* and *Sca1::PV*, and Pearson's correlation.
(H) Q.A. of anterior (lobules II–V) and posterior (lobules VI–X) cerebellum for Frrs1l expression in MLINs.
(I) R.I. of GluR2 and Q.A. displaying increased GluR2 expression in *Sca1::PV* MLINs vs. WT::*PV*. n = 3–5 mice for analysis. Graphs (B and G) represent mean ± SEM, (I) depicts mean values/animal, *p < 0.05, **p < 0.01, ***p < 0.001. Scale bars, (G) 20, (I) 5 (μm). See also Figure S13 and Table S1.

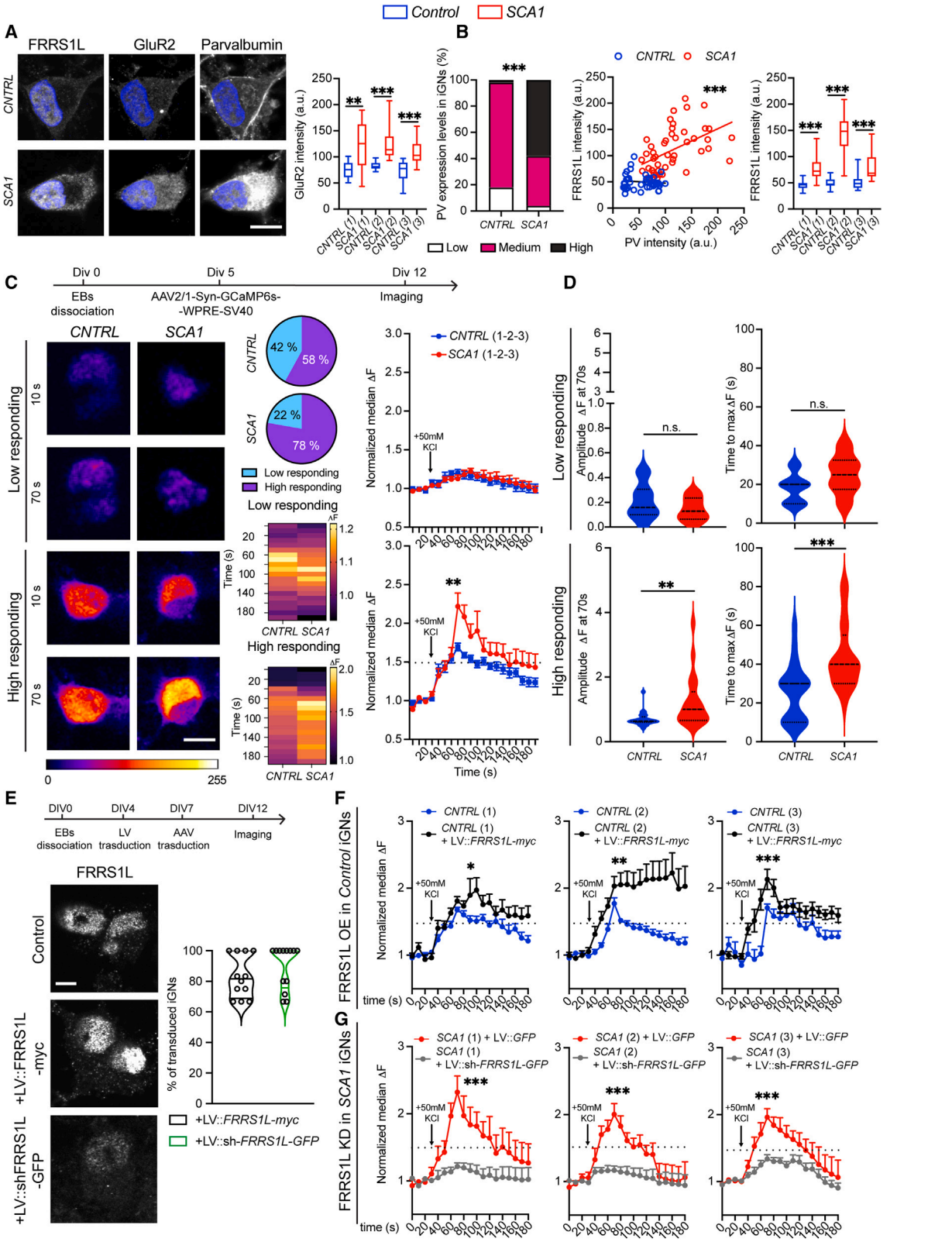

(legend on next page)

activity and similar to GoI drive vicious loops of MLIN hyperactivation.

Our study reveals that altered GABAergic inputs can causally contribute to circuit-level dysfunctions. Notably, reducing GABA transmission also restored PN pacemaker activity in an ethanol-exposure model.[56] The selective lowering of the inhibitory tone by chemogenetically silencing *Sca1* MLINs in our study, lead to an immediate improvement in motor performance. This rapid improvement suggests that the *Sca1* phenotype is not primarily due to PN degeneration, and importantly highlights the therapeutic potential of this cell-type-specific intervention. Intriguingly, acute chemogenetic-mediated MLIN silencing significantly reduces the hyperexcitability of PN dendrites, indicating that this hitherto believed PN cell-autonomous alteration might, at least in part, constitute a maladaptive feature in response to excess MLIN-mediated inhibition.

However, MLIN hyperexcitability is not the sole driver of PN degeneration, especially as ample evidences point to PN cell-autonomous processes.[57,58] Nevertheless, recent studies highlight alterations in non-cell autonomous processes, synergistically enhancing or even initiating dysfunction within PNs. Excitatory PF-PN and CF-PN synaptic dysfunctions are observed in rodent models of SCAs, indicating a conserved role for circuit elements in either triggering or governing cerebellar neurodegeneration. Specifically, these alterations could affect intrinsic PN excitability, as well as alter synaptic responses.[14,59–61] Ataxin-1 controls the expression of $Ca_v3.1$ and TRPC3 channels, involved in the regulation of intrinsic PN excitability, and mutant Ataxin-1 renders PNs hyperexcitable in a cell-autonomous fashion.[30] Therefore, homeostatic mechanisms in response to excess MLIN-mediated inhibition might lead to further reductions in the expression of these receptors and anticipate PN degeneration.

Our chemogenetically mediated MLIN stimulation in healthy mice highlights the pivotal role for this circuit element in driving motor deficits typical of SCA1. Importantly, it demonstrates the vulnerability of PNs to extended periods of excessive inhibition, which causes long-term synaptic deficits on PNs, and, on a longer time scale, might cause overt PN degeneration. An interesting pathophysiological overlap exists with Episodic Ataxia type 1 (EA1), characterized by stress-induced attacks of spastic contractions and motor dysfunction. EA1 is a channelopathy, causing increased inhibitory synaptic input on PNs, particularly at pinceau synapses, thus strongly regulating action potential generation.[62] Despite a striking similarity to SCA1, with regard to excessive MLIN-mediated inhibition of PNs, EA1 lacks neurodegeneration, likely due to unaltered basket cell firing.[63] Notably, altered excitability of PV-interneurons has been reported in other neurological diseases.[64–68] In Alzheimer's disease, interneuron-deficits not only underlie cognitive decline but also epileptic discharges.[68,69] In Dravet syndrome, PV-interneurons exhibit impaired excitability, thus participating in disease pathophysiology.[70] In ALS and Fragile-X syndrome, PV-interneurons are hypoexcitable, thereby causing cortical hyperexcitability.[66,71] SCA1, however, represents a special case, as MLINs turn hyperexcitable. But why are MLINs hyperexcitable? We show that homotypic synaptic connections are altered, likely resulting in defective reciprocal inhibition among the MLIN population. Moreover, in *Sca1* mice, we found strongly increased levels of the calcium buffer PV and lowered resting cytoplasmic calcium concentrations, which recently have been linked to increased neuronal excitability.[72] We propose that altered calcium homeostasis observed in *Sca1* MLINs contribute toward higher MLIN activity. Patient-derived iGNs experiments also argue for intrinsic alterations, and our proteomic analyses identified alterations in synaptic molecules, which might contribute to altered MLIN synaptic function and neurotransmission.

FRRS1L is a recently identified, predominantly brain-localized protein, with the highest expression in the cortex, cerebellum, hippocampus, and basal-ganglia.[73] Patients harboring recessive loss-of-function mutations in *FRRS1L* gene, exhibit severe intellectual disability, movement disorders, hypotonia, and epilepsy.[39,73,74] Notably, some patients manifest cortical and cerebellar neurodegeneration. FRRS1L within the ER regulates AMPA receptor assembly via FRRS1l/CPT1c complexes, enabling multimer-formation of GluAs and their trafficking to the plasma membrane.[75] In *Sca1* mice and in patient iGNs, a selective increase in FRRS1L levels indicate that FRRS1L levels can influence synaptic plasticity and shape activity patterns. Importantly, FRRSIL overexpression in *CNTRL* iGNs alters their intrinsic properties, rendering them hyperresponsive to depolarizing stimulation. However, future studies are needed to decipher how Ataxin-1 contributes to altered FRRS1L expression. One likely pathway for future investigation is that of Sirtuin-1,

Figure 8. iGNs activity in *Control* and *SCA1* correlates with PV and FRRS1L expression

(A) R.I. of FRRS1L, GluR2 and PV expression in 3 human *SCA1* patients' iPSC-derived iGNs vs. 3 *CNTRL* lines and Q.A. of elevated. GluR2 expression.

(B) Q.A. of PV expression binned into expression classes: high, medium, and low (chi-squared test). Pearson's correlation between PV expression and FRRS1L in *SCA1* vs. *CNTRL*. Q.A. of FRRS1L expression level.

(C) Experimental timeline for iGNs calcium imaging and Q.A. of differentially responding populations after 50 mM KCl stimulation (low-responding cut off: 1–1.5 at 70 s; high-responding < 1.5 at 70 s) and corresponding heatmaps. Q.A. of calcium transients showing increase in ΔF at 70 s in *SCA1* high-responding neurons vs. *CNTRL*.

(D) Significant increase in ΔF amplitude at 70 s in *SCA1* high-responding neurons. Time to max ΔF was significantly higher in high-responding *SCA1* populations. n = 27–33 neurons.

(E) Timeline for calcium imaging of iGNs transduced at DIV4 with LV:*FRRS1L*-myc (transduction efficiency, mean: 83.06) or LV:sh*FRRS1L*-GFP (transduction efficiency mean: 89.60) or LV-GFP. Subsequently at DIV7 iGNs were infected with AAV2/1-GCaMP6 or AAV2/1-RCaMP. R.I. of FRRS1L overexpression or knockdown in iGNs.

(F) Q.A. of calcium transients in *CNTRL* lines overexpressing FRRS1L, showing increase in ΔF after KCl stimulation, n = 12–15 neurons/condition.

(G) Q.A. of calcium transients in *SCA1* lines after *FRRS1L* knockdown, displaying decline in ΔF after KCl stimulation. n = 12–14 neurons/condition. Box and whisker plot in (A and B) and graphs in (C and F) show mean ± SEM, (E) percentage of mean/coverslip. *p < 0.05, **p < 0.01, ***p < 0.001. Scale bars, (A, B, and D) 15 μm. See also Figures S14 and S15.

which normalizes calcium homeostasis, thus promoting neuroprotection in SCA7.[76]

Lastly, our findings present new evidence for early cerebellar circuit-related dysfunction in SCA1 and provide important insight into enhanced inhibitory drive onto PNs triggering molecular pathology, which induces PN degeneration. Our work highlights brain state-dependent alterations within the cerebellar circuit, and, to our knowledge, for the first time, it implicates early deficits in sensorimotor processing as a potential diagnostic hallmark of SCA1.

STAR★METHODS

Detailed methods are provided in the online version of this paper and include the following:

- KEY RESOURCES TABLE
- RESOURCE AVAILABILITY
  - Lead contact
  - Materials availability
  - Data and code availability
- EXPERIMENTAL MODEL AND SUBJECT DETAILS
  - Mice strains
- METHOD DETAILS
  - Pharmacological treatments
  - Accelerating Rotarod
  - Hindlimb clasping assay
  - DREADDs and genetically encoded calcium indicators for *in vivo* imaging
  - Intracerebroventricular (i.c.v.) injection
  - Surgical procedures in adult animals at UBERN
  - Cranial window implantation and virus injection at LMU
  - Two-photon imaging in awake and anesthetized mice
  - Ratiometric calcium imaging
  - Chronic CNO treatment at LMU-UBERN
  - Calcium imaging with acute CNO administration
  - Immunofluorescence of rodent tissue at UBERN
  - Confocal microscopy
  - SBF-SEM
  - iPSC differentiation into GABAergic neurons (iGNs)
  - Immunofluorescence staining of iGNs
  - FACS of MLIN
  - Mass spectrometry of sorted MLIN
  - Calcium imaging of iGNs and lentiviral-mediated FRRS1l transduction
- QUANTIFICATION AND STATISTICAL ANALYSIS
  - Microscopy and image analysis
  - Data analysis of mass spectrometry
  - *In vivo* two-photon calcium image processing and data analysis
  - Population activity dimensionality and manifold analysis
  - Statistical analysis

SUPPLEMENTAL INFORMATION

Supplemental information can be found online at https://doi.org/10.1016/j.neuron.2023.05.016.

ACKNOWLEDGMENTS

We are grateful to all the SCA1 patients and their families united in the Dutch SCA1 Families Fund for donating fibroblasts (Leiden). We thank Shenyi Jiang (LMU) for confocal microscopy and Angelina Oestmann (UBERN) for taking care of the animals. The study was supported by the European Research Council under the European Union's Horizon 2020 research and innovation program (#725825), SAND: Marie Skłodowska-Curie actions, Innovative Training Network, and E-rare grant (CALSER) to S.S, and German Research Foundation under Germany's Excellence Strategy within the framework of the Munich Cluster for Systems Neurology -EXC 2145 SyNergy- ID 390857198, and the Emmy Noether Program to S. Liebscher.

AUTHOR CONTRIBUTIONS

Conceptualization and writing, F.P., S.S., and S. Liebscher; investigation and analyses, F.P., C.D., R.D., X.Y., Z.A.Q., A.O., C.T., M.M., and A.T.; FACS, mass spectrometry, and analyses, S.M., S. Lagache, A.C.U., and M.H.; reagents, R.A.M.B., W.M.C.v.R.-M., and B.Z.; supervision, S.S. and S. Liebscher.

DECLARATION OF INTERESTS

The authors declare no competing interests.

INCLUSION AND DIVERSITY

One or more of the authors of this paper self-identifies as an underrepresented ethnic minority in their field of research or within their geographical location. One or more of the authors of this paper self-identifies as a gender minority in their field of research. One or more of the authors of this paper self-identifies as a member of the LGBTQIA+ community.

Received: September 14, 2022
Revised: March 17, 2023
Accepted: May 17, 2023
Published: June 14, 2023

REFERENCES

1. Leroy, F., and Zytnicki, D. (2015). Is hyperexcitability really guilty in amyotrophic lateral sclerosis? Neural Regen. Res. *10*, 1413–1415. https://doi.org/10.4103/1673-5374.165308.
2. Roselli, F., and Caroni, P. (2015). From intrinsic firing properties to selective neuronal vulnerability in neurodegenerative diseases. Neuron *85*, 901–910. https://doi.org/10.1016/j.neuron.2014.12.063.
3. Mentis, G.Z., Blivis, D., Liu, W., Drobac, E., Crowder, M.E., Kong, L., Alvarez, F.J., Sumner, C.J., and O'Donovan, M.J. (2011). Early functional impairment of sensory-motor connectivity in a mouse model of spinal muscular atrophy. Neuron *69*, 453–467. https://doi.org/10.1016/j.neuron.2010.12.032.
4. Leroy, F., Lamotte d'Incamps, B., Imhoff-Manuel, R.D., and Zytnicki, D. (2014). Early intrinsic hyperexcitability does not contribute to motoneuron degeneration in amyotrophic lateral sclerosis. eLife *3*. https://doi.org/10.7554/eLife.04046.
5. Saxena, S., Roselli, F., Singh, K., Leptien, K., Julien, J.P., Gros-Louis, F., and Caroni, P. (2013). Neuroprotection through excitability and mTOR required in ALS motoneurons to delay disease and extend survival. Neuron *80*, 80–96. https://doi.org/10.1016/j.neuron.2013.07.027.
6. Barnes, J.A., Ebner, B.A., Duvick, L.A., Gao, W., Chen, G., Orr, H.T., and Ebner, T.J. (2011). Abnormalities in the climbing fiber-Purkinje cell circuitry contribute to neuronal dysfunction in ATXN1[82Q] mice. J. Neurosci. *31*, 12778–12789. https://doi.org/10.1523/JNEUROSCI.2579-11.2011.
7. Hansen, S.T., Meera, P., Otis, T.S., and Pulst, S.M. (2013). Changes in Purkinje cell firing and gene expression precede behavioral pathology in a mouse model of SCA2. Hum. Mol. Genet. *22*, 271–283. https://doi.org/10.1093/hmg/dds427.

8. Paulson, H.L., Shakkottai, V.G., Clark, H.B., and Orr, H.T. (2017). Polyglutamine spinocerebellar ataxias — from genes to potential treatments. Nat. Rev. Neurosci. *18*, 613–626. https://doi.org/10.1038/nrn.2017.92.

9. Braz, B.Y., Wennagel, D., Ratié, L., de Souza, D.A.R., Deloulme, J.C., Barbier, E.L., Buisson, A., Lanté, F., and Humbert, S. (2022). Treating early postnatal circuit defect delays Huntington's disease onset and pathology in mice. Science *377*, eabq5011. https://doi.org/10.1126/science.abq5011.

10. Pradhan, J., and Bellingham, M.C. (2021). Neurophysiological mechanisms underlying cortical hyper-excitability in amyotrophic lateral sclerosis: a review. Brain Sci. *11*, 549. https://doi.org/10.3390/brainsci11050549.

11. Ramírez-Jarquín, U.N., Lazo-Gómez, R., Tovar-y-Romo, L.B., and Tapia, R. (2014). Spinal inhibitory circuits and their role in motor neuron degeneration. Neuropharmacology *82*, 101–107. https://doi.org/10.1016/j.neuropharm.2013.10.003.

12. Gunes, Z.I., Kan, V.W.Y., Ye, X., and Liebscher, S. (2020). Exciting complexity: the role of motor circuit elements in ALS pathophysiology. Front. Neurosci. *14*, 573. https://doi.org/10.3389/fnins.2020.00573.

13. Edamakanti, C.R., Do, J., Didonna, A., Martina, M., and Opal, P. (2018). Mutant ataxin1 disrupts cerebellar development in spinocerebellar ataxia type 1. J. Clin. Invest. *128*, 2252–2265. https://doi.org/10.1172/JCI96765.

14. Ruegsegger, C., Stucki, D.M., Steiner, S., Angliker, N., Radecke, J., Keller, E., Zuber, B., Rüegg, M.A., and Saxena, S. (2016). Impaired mTORC1-dependent expression of Homer-3 influences SCA1 pathophysiology. Neuron *89*, 129–146. https://doi.org/10.1016/j.neuron.2015.11.033.

15. Duvick, L., Barnes, J., Ebner, B., Agrawal, S., Andresen, M., Lim, J., Giesler, G.J., Zoghbi, H.Y., and Orr, H.T. (2010). SCA1-like disease in mice expressing wild-type ataxin-1 with a serine to aspartic acid replacement at residue 776. Neuron *67*, 929–935. https://doi.org/10.1016/j.neuron.2010.08.022.

16. Ebner, B.A., Ingram, M.A., Barnes, J.A., Duvick, L.A., Frisch, J.L., Clark, H.B., Zoghbi, H.Y., Ebner, T.J., and Orr, H.T. (2013). Purkinje cell ataxin-1 modulates climbing fiber synaptic input in developing and adult mouse cerebellum. J. Neurosci. *33*, 5806–5820. https://doi.org/10.1523/JNEUROSCI.6311-11.2013.

17. Kim, J., and Augustine, G.J. (2021). Molecular layer interneurons: key elements of cerebellar network computation and behavior. Neuroscience *462*, 22–35. https://doi.org/10.1016/j.neuroscience.2020.10.008.

18. Vig, P.J., Fratkin, J.D., Desaiah, D., Currier, R.D., and Subramony, S.H.. (1996). Decreased parvalbumin immunoreactivity in surviving Purkinje cells of patients with spinocerebellar ataxia-1. Neurology *47*, 249–253. https://doi.org/10.1212/wnl.47.1.249.

19. Chen, T.W., Wardill, T.J., Sun, Y., Pulver, S.R., Renninger, S.L., Baohan, A., Schreiter, E.R., Kerr, R.A., Orger, M.B., Jayaraman, V., et al. (2013). Ultrasensitive fluorescent proteins for imaging neuronal activity. Nature *499*, 295–300. https://doi.org/10.1038/nature12354.

20. Dana, H., Sun, Y., Mohar, B., Hulse, B.K., Kerlin, A.M., Hasseman, J.P., Tsegaye, G., Tsang, A., Wong, A., Patel, R., et al. (2019). High-performance calcium sensors for imaging activity in neuronal populations and microcompartments. Nat. Methods *16*, 649–657. https://doi.org/10.1038/s41592-019-0435-6.

21. Raman, I.M., and Bean, B.P. (1999). Ionic currents underlying spontaneous action potentials in isolated cerebellar Purkinje neurons. J. Neurosci. *19*, 1663–1674. https://doi.org/10.1523/JNEUROSCI.19-05-01663.1999.

22. Ramirez, J.E., and Stell, B.M. (2016). Calcium imaging reveals coordinated simple spike pauses in populations of cerebellar Purkinje cells. Cell Rep. *17*, 3125–3132. https://doi.org/10.1016/j.celrep.2016.11.075.

23. Thestrup, T., Litzlbauer, J., Bartholomäus, I., Mues, M., Russo, L., Dana, H., Kovalchuk, Y., Liang, Y., Kalamakis, G., Laukat, Y., et al. (2014). Optimized ratiometric calcium sensors for functional in vivo imaging of neurons and T lymphocytes. Nat. Methods *11*, 175–182. https://doi.org/10.1038/nmeth.2773.

24. Dell'Orco, J.M., Wasserman, A.H., Chopra, R., Ingram, M.A.C., Hu, Y.S., Singh, V., Wulff, H., Opal, P., Orr, H.T., and Shakkottai, V.G. (2015). Neuronal atrophy early in degenerative ataxia is a compensatory mechanism to regulate membrane excitability. J. Neurosci. *35*, 11292–11307. https://doi.org/10.1523/JNEUROSCI.1357-15.2015.

25. Gurnani, H., and Silver, R.A. (2021). Multidimensional population activity in an electrically coupled inhibitory circuit in the cerebellar cortex. Neuron *109*. 1739.e8–1753.e8. https://doi.org/10.1016/j.neuron.2021.03.027.

26. Cayco-Gajic, N.A., and Silver, R.A. (2019). Re-evaluating circuit mechanisms underlying pattern separation. Neuron *101*, 584–602. https://doi.org/10.1016/j.neuron.2019.01.044.

27. Lanore, F., Cayco-Gajic, N.A., Gurnani, H., Coyle, D., and Silver, R.A. (2021). Cerebellar granule cell axons support high-dimensional representations. Nat. Neurosci. *24*, 1142–1150. https://doi.org/10.1038/s41593-021-00873-x.

28. Gobbo, F., Mitchell-Heggs, R., and Tse, D. (2022). Changes in brain activity and connectivity as memories age. Cogn. Neurosci. *13*, 141–143. https://doi.org/10.1080/17588928.2022.2076076.

29. Vyas, S., Golub, M.D., Sussillo, D., and Shenoy, K.V. (2020). Computation through neural population dynamics. Annu. Rev. Neurosci. *43*, 249–275. https://doi.org/10.1146/annurev-neuro-092619-094115.

30. Chopra, R., Bushart, D.D., Cooper, J.P., Yellajoshyula, D., Morrison, L.M., Huang, H., Handler, H.P., Man, L.J., Dansithong, W., Scoles, D.R., et al. (2020). Altered Capicua expression drives regional Purkinje neuron vulnerability through ion channel gene dysregulation in spinocerebellar ataxia type 1. Hum. Mol. Genet. *29*, 3249–3265. https://doi.org/10.1093/hmg/ddaa212.

31. Wagner, M.J., Savall, J., Hernandez, O., Mel, G., Inan, H., Rumyantsev, O., Lecoq, J., Kim, T.H., Li, J.Z., Ramakrishnan, C., et al. (2021). A neural circuit state change underlying skilled movements. Cell *184*. 3731.e21–3747.e21. https://doi.org/10.1016/j.cell.2021.06.001.

32. Donato, F., Rompani, S.B., and Caroni, P. (2013). Parvalbumin-expressing basket-cell network plasticity induced by experience regulates adult learning. Nature *504*, 272–276. https://doi.org/10.1038/nature12866.

33. Donato, F., Chowdhury, A., Lahr, M., and Caroni, P. (2015). Early- and late-born parvalbumin basket cell subpopulations exhibiting distinct regulation and roles in learning. Neuron *85*, 770–786. https://doi.org/10.1016/j.neuron.2015.01.011.

34. Wang, W.X., Qiao, J., and Lefebvre, J.L. (2022). PV-IRES-Cre mouse line targets excitatory granule neurons in the cerebellum. Mol. Brain *15*, 85. https://doi.org/10.1186/s13041-022-00972-1.

35. Vig, P.J.S., Subramony, S.H., Burright, E.N., Fratkin, J.D., McDaniel, D.O., Desaiah, D., and Qin, Z. (1998). Reduced immunoreactivity to calcium-binding proteins in Purkinje cells precedes onset of ataxia in spinocerebellar ataxia-1 transgenic mice. Neurology *50*, 106–113. https://doi.org/10.1212/WNL.50.1.106.

36. Ma, M., Futia, G.L., de Souza, F.M.S., Ozbay, B.N., Llano, I., Gibson, E.A., and Restrepo, D. (2020). Molecular layer interneurons in the cerebellum encode for valence in associative learning. Nat. Commun. *11*, 4217. https://doi.org/10.1038/s41467-020-18034-2.

37. Cvetanovic, M., Ingram, M., Orr, H., and Opal, P. (2015). Early activation of microglia and astrocytes in mouse models of spinocerebellar ataxia type 1. Neuroscience *289*, 289–299. https://doi.org/10.1016/j.neuroscience.2015.01.003.

38. Buijsen, R.A.M., Gardiner, S.L., Bouma, M.J., van der Graaf, L.M., Boogaard, M.W., Pepers, B.A., Eussen, B., de Klein, A., Freund, C., and van Roon-Mom, W.M.C. (2018). Generation of 3 spinocerebellar ataxia type 1 (SCA1) patient-derived induced pluripotent stem cell lines LUMCi002-A, B, and C and 2 unaffected sibling control induced pluripotent stem cell lines LUMCi003-A and B. Stem Cell Res. *29*, 125–128. https://doi.org/10.1016/j.scr.2018.03.018.

39. Brechet, A., Buchert, R., Schwenk, J., Boudkkazi, S., Zolles, G., Siquier-Pernet, K., Schaber, I., Bildl, W., Saadi, A., Bole-Feysot, C., et al. (2017).

AMPA-receptor specific biogenesis complexes control synaptic transmission and intellectual ability. Nat. Commun. *8*, 15910. https://doi.org/10.1038/ncomms15910.

40. Kozareva, V., Martin, C., Osorno, T., Rudolph, S., Guo, C., Vanderburg, C., Nadaf, N., Regev, A., Regehr, W.G., and Macosko, E. (2021). A transcriptomic atlas of mouse cerebellar cortex comprehensively defines cell types. Nature *598*, 214–219. https://doi.org/10.1038/s41586-021-03220-z.

41. Cendelin, J. (2014). From mice to men: lessons from mutant ataxic mice. Cerebellum. Ataxias *1*, 4. https://doi.org/10.1186/2053-8871-1-4.

42. Gaffield, M.A., and Christie, J.M. (2017). Movement rate is encoded and influenced by widespread, coherent activity of cerebellar molecular layer interneurons. J. Neurosci. *37*, 4751–4765. https://doi.org/10.1523/JNEUROSCI.0534-17.2017.

43. Astorga, G., Li, D., Therreau, L., Kassa, M., Marty, A., and Llano, I. (2017). Concerted interneuron activity in the cerebellar molecular layer during rhythmic oromotor behaviors. J. Neurosci. *37*, 11455–11468. https://doi.org/10.1523/JNEUROSCI.1091-17.2017.

44. Heiney, S.A., Wohl, M.P., Chettih, S.N., Ruffolo, L.I., and Medina, J.F. (2014). Cerebellar-dependent expression of motor learning during eyeblink conditioning in head-fixed mice. J. Neurosci. *34*, 14845–14853. https://doi.org/10.1523/JNEUROSCI.2820-14.2014.

45. D'Angelo, E., and Casali, S. (2012). Seeking a unified framework for cerebellar function and dysfunction: from circuit operations to cognition. Front. Neural Circuits *6*, 116. https://doi.org/10.3389/fncir.2012.00116.

46. Duguid, I., Branco, T., Chadderton, P., Arlt, C., Powell, K., and Häusser, M. (2015). Control of cerebellar granule cell output by sensory-evoked Golgi cell inhibition. Proc. Natl. Acad. Sci. USA *112*, 13099–13104. https://doi.org/10.1073/pnas.1510249112.

47. D'Angelo, E., and De Zeeuw, C.I. (2009). Timing and plasticity in the cerebellum: focus on the granular layer. Trends Neurosci. *32*, 30–40. https://doi.org/10.1016/j.tins.2008.09.007.

48. Arancillo, M., White, J.J., Lin, T., Stay, T.L., and Sillitoe, R.V. (2015). In vivo analysis of Purkinje cell firing properties during postnatal mouse development. J. Neurophysiol. *113*, 578–591. https://doi.org/10.1152/jn.00586.2014.

49. Serra, H.G., Duvick, L., Zu, T., Carlson, K., Stevens, S., Jorgensen, N., Lysholm, A., Burright, E., Zoghbi, H.Y., Clark, H.B., et al. (2006). RORα-mediated Purkinje cell development determines disease severity in adult SCA1 mice. Cell *127*, 697–708. https://doi.org/10.1016/j.cell.2006.09.036.

50. Morino, H., Matsuda, Y., Muguruma, K., Miyamoto, R., Ohsawa, R., Ohtake, T., Otobe, R., Watanabe, M., Maruyama, H., Hashimoto, K., et al. (2015). A mutation in the low voltage-gated calcium channel CACNA1G alters the physiological properties of the channel, causing spinocerebellar ataxia. Mol. Brain *8*, 89. https://doi.org/10.1186/s13041-015-0180-4.

51. Riess, O., Schöls, L., Bottger, H., Nolte, D., Vieira-Saecker, A.M., Schimming, C., Kreuz, F., Macek, M., Krebsová, A., Macek, M.S., et al. (1997). SCA6 is caused by moderate CAG expansion in the alpha1A-voltage-dependent calcium channel gene. Hum. Mol. Genet. *6*, 1289–1293. https://doi.org/10.1093/hmg/6.8.1289.

52. Niewiadomska-Cimicka, A., Doussau, F., Perot, J.B., Roux, M.J., Keime, C., Hache, A., Piguet, F., Novati, A., Weber, C., Yalcin, B., et al. (2021). SCA7 mouse cerebellar pathology reveals preferential downregulation of key Purkinje cell-identity genes and shared disease signature with SCA1 and SCA2. J. Neurosci. *41*, 4910–4936. https://doi.org/10.1523/JNEUROSCI.1882-20.2021.

53. Rajakulendran, S., Schorge, S., Kullmann, D.M., and Hanna, M.G. (2010). Dysfunction of the Ca(V)2.1 calcium channel in cerebellar ataxias. F1000 Biol. Rep. *2*.

54. Pietrobon, D. (2010). CAv2.1 channelopathies. Pflugers Arch. *460*, 375–393. https://doi.org/10.1007/s00424-010-0802-8.

55. Sendhilnathan, N., Goldberg, M.E., and Ipata, A.E. (2022). Mixed selectivity in the cerebellar Purkinje-cell response during visuomotor association learning. J. Neurosci. *42*, 3847–3855. https://doi.org/10.1523/JNEUROSCI.1771-21.2022.

56. Dong, G.H., Xu, Y.H., Liu, L.Y., Lu, D., Chu, C.P., Cui, S.B., and Qiu, D.L. (2022). Chronic ethanol exposure during adolescence impairs simple spike activity of cerebellar Purkinje cells in vivo in mice. Neurosci. Lett. *771*, 136396. https://doi.org/10.1016/j.neulet.2021.136396.

57. Pérez Ortiz, J.M., and Orr, H.T. (2018). Spinocerebellar ataxia type 1: molecular mechanisms of neurodegeneration and preclinical studies, pp. 135–145. https://doi.org/10.1007/978-3-319-71779-1_6.

58. Ju, H., Kokubu, H., and Lim, J. (2014). Beyond the glutamine expansion: influence of posttranslational modifications of ataxin-1 in the pathogenesis of spinocerebellar ataxia Type 1. Mol. Neurobiol. *50*, 866–874. https://doi.org/10.1007/s12035-014-8703-z.

59. Kuo, S.H., Lin, C.Y., Wang, J., Sims, P.A., Pan, M.K., Liou, J.-Y., Lee, D., Tate, W.J., Kelly, G.C., Louis, E.D., et al. (2017). Climbing fiber-Purkinje cell synaptic pathology in tremor and cerebellar degenerative diseases. Acta. Neuropathol. *133*, 121–138. https://doi.org/10.1007/s00401-016-1626-1.

60. Shuvaev, A.N., Belozor, O.S., Mozhei, O.I., Shuvaev, A.N., Fritsler, Y.V., Khilazheva, E.D., Mosyagina, A.I., Hirai, H., Teschemacher, A.G., and Kasparov, S. (2022). Indirect negative effect of mutant ataxin-1 on short- and long-term synaptic plasticity in mouse models of spinocerebellar ataxia type 1. Cells *11*, 2247. https://doi.org/10.3390/cells11142247.

61. Hoxha, E., Balbo, I., Miniaci, M.C., and Tempia, F. (2018). Purkinje cell signaling deficits in animal models of ataxia. Front. Synaptic Neurosci. *10*, 6. https://doi.org/10.3389/fnsyn.2018.00006.

62. D'Adamo, M.C., Hasan, S., Guglielmi, L., Servettini, I., Cenciarini, M., Catacuzzeno, L., and Franciolini, F. (2015). New insights into the pathogenesis and therapeutics of episodic ataxia type 1. Front. Cell. Neurosci. *9*, 317. https://doi.org/10.3389/fncel.2015.00317.

63. Herson, P.S., Virk, M., Rustay, N.R., Bond, C.T., Crabbe, J.C., Adelman, J.P., and Maylie, J. (2003). A mouse model of episodic ataxia type-1. Nat. Neurosci. *6*, 378–383. https://doi.org/10.1038/nn1025.

64. Ferguson, B.R., and Gao, W.J. (2018). Pv interneurons: critical regulators of E/I balance for prefrontal cortex-dependent behavior and psychiatric disorders. Front. Neural Circuits *12*, 37. https://doi.org/10.3389/fncir.2018.00037.

65. Hijazi, S., Heistek, T.S., Scheltens, P., Neumann, U., Shimshek, D.R., Mansvelder, H.D., Smit, A.B., and van Kesteren, R.E. (2020). Early restoration of parvalbumin interneuron activity prevents memory loss and network hyperexcitability in a mouse model of Alzheimer's disease. Mol. Psychiatry *25*, 3380–3398. https://doi.org/10.1038/s41380-019-0483-4.

66. Khademullah, C.S., Aqrabawi, A.J., Place, K.M., Dargaei, Z., Liang, X., Pressey, J.C., Bedard, S., Yang, J.W., Garand, D., Keramidis, I., et al. (2020). Cortical interneuron-mediated inhibition delays the onset of amyotrophic lateral sclerosis. Brain *143*, 800–810. https://doi.org/10.1093/brain/awaa034.

67. Morello, N., Schina, R., Pilotto, F., Phillips, M., Melani, R., Plicato, O., Pizzorusso, T., Pozzo-Miller, L., and Giustetto, M. (2018). Loss of *Mecp2* causes atypical synaptic and molecular plasticity of parvalbumin-expressing interneurons reflecting Rett syndrome–like sensorimotor defects. eNeuro *5*, 0086–18.2018. eNeuro. https://doi.org/10.1523/ENEURO.0086-18.2018.

68. Palop, J.J., Jones, B., Kekonius, L., Chin, J., Yu, G.Q., Raber, J., Masliah, E., and Mucke, L. (2003). Neuronal depletion of calcium-dependent proteins in the dentate gyrus is tightly linked to Alzheimer's disease-related cognitive deficits. Proc. Natl. Acad. Sci. USA *100*, 9572–9577. https://doi.org/10.1073/pnas.1133381100.

69. Verret, L., Mann, E.O., Hang, G.B., Barth, A.M.I., Cobos, I., Ho, K., Devidze, N., Masliah, E., Kreitzer, A.C., Mody, I., et al. (2012). Inhibitory interneuron deficit links altered network activity and cognitive dysfunction

in Alzheimer model. Cell *149*, 708–721. https://doi.org/10.1016/j.cell.2012.02.046.

70. Tai, C., Abe, Y., Westenbroek, R.E., Scheuer, T., and Catterall, W.A. (2014). Impaired excitability of somatostatin- and parvalbumin-expressing cortical interneurons in a mouse model of Dravet syndrome. Proc. Natl. Acad. Sci. USA *111*, E3139–E3148. https://doi.org/10.1073/pnas.1411131111.
71. Liu, X., Kumar, V., Tsai, N.P., and Auerbach, B.D. (2021). Hyperexcitability and homeostasis in fragile X syndrome. Front. Mol. Neurosci. *14*, 805929. https://doi.org/10.3389/fnmol.2021.805929.
72. Paeger, L., Pippow, A., Hess, S., Paehler, M., Klein, A.C., Husch, A., Pouzat, C., Brüning, J.C., and Kloppenburg, P. (2017). Energy imbalance alters Ca2+ handling and excitability of POMC neurons. eLife *6*. https://doi.org/10.7554/eLife.25641.
73. Madeo, M., Stewart, M., Sun, Y., Sahir, N., Wiethoff, S., Chandrasekar, I., Yarrow, A., Rosenfeld, J.A., Yang, Y., Cordeiro, D., et al. (2016). Loss-of-function mutations in FRRS1L lead to an epileptic-dyskinetic encephalopathy. Am. J. Hum. Genet. *98*, 1249–1255. https://doi.org/10.1016/j.ajhg.2016.04.008.
74. Shaheen, R., Al Tala, S., Ewida, N., Abouelhoda, M., and Alkuraya, F.S. (2016). Epileptic encephalopathy with continuous spike-and-wave during sleep maps to a homozygous truncating mutation in AMPA receptor component FRRS1L. Clin. Genet. *90*, 282–283. https://doi.org/10.1111/cge.12796.
75. Schwenk, J., Boudkkazi, S., Kocylowski, M.K., Brechet, A., Zolles, G., Bus, T., Costa, K., Kollewe, A., Jordan, J., Bank, J., et al. (2019). An ER assembly line of AMPA-receptors controls excitatory neurotransmission and its plasticity. Neuron *104*. 680.e9–692.e9. https://doi.org/10.1016/j.neuron.2019.08.033.
76. Stoyas, C.A., Bushart, D.D., Switonski, P.M., Ward, J.M., Alaghatta, A., Tang, M.B., Niu, C., Wadhwa, M., Huang, H., Savchenko, A., et al. (2020). Nicotinamide pathway-dependent Sirt1 activation restores calcium homeostasis to achieve neuroprotection in spinocerebellar ataxia type 7. Neuron *105*, 630–644.e9. https://doi.org/10.1016/j.neuron.2019.11.019.
77. Krashes, M.J., Koda, S., Ye, C., Rogan, S.C., Adams, A.C., Cusher, D.S., Maratos-Flier, E., Roth, B.L., and Lowell, B.B. (2011). Rapid, reversible activation of AgRP neurons drives feeding behavior in mice. J Clin Invest *121*, 1424–1428. https://doi.org/10.1172/JCI46229.
78. Dana, H., Mohar, B., Sun, Y., Narayan, S., Gordus, A., Hasseman, J.P., Tsegaye, G., Holt, G.T., Hu, A., Walpita, D., et al. (2016). Sensitive red protein calcium indicators for imaging neural activity. Elife *5*, e12727. https://doi.org/10.7554/eLife.12727.
79. Kremer, J.R., Mastronarde, D.N., and McIntosh, J.R. (1996). Computer visualization of three-dimensional image data using IMOD. J Struct Biol *116*, 71–76. https://doi.org/10.1006/jsbi.1996.0013.
80. Keller, G.B., Bonhoeffer, T., and Hübener, M. (2012). Sensorimotor mismatch signals in primary visual cortex of the behaving mouse. Neuron *74*, 809–815. https://doi.org/10.1016/j.neuron.2012.03.040.
81. Watase, K., Weeber, E.J., Xu, B., Antalffy, B., Yuva-Paylor, L., Hashimoto, K., Kano, M., Atkinson, R., Sun, Y., Armstrong, D.L., et al. (2002). A long CAG repeat in the mouse Sca1 locus replicates SCA1 features and reveals the impact of protein solubility on selective neurodegeneration. Neuron *34*, 905–919. https://doi.org/10.1016/S0896-6273(02)00733-X.
82. Urban, D.J., Zhu, H., Marcinkiewcz, C.A., Michaelides, M., Oshibuchi, H., Rhea, D., Aryal, D.K., Farrell, M.S., Lowery-Gionta, E., Olsen, R.H.J., et al. (2016). Elucidation of the behavioral program and neuronal network encoded by dorsal raphe serotonergic neurons. Neuropsychopharmacology *41*, 1404–1415. https://doi.org/10.1038/npp.2015.293.
83. Dirren, E., Towne, C.L., Setola, V., Redmond, D.E., Schneider, B.L., and Aebischer, P. (2014). Intracerebroventricular injection of adeno-associated virus 6 and 9 vectors for cell type–specific transgene expression in the spinal cord. Hum. Gene Ther. *25*, 109–120. https://doi.org/10.1089/hum.2013.021.
84. Walton, J. (1979). Lead aspartate, an en bloc contrast stain particularly useful for ultrastructural enzymology. J. Histochem. Cytochem. *27*, 1337–1342. https://doi.org/10.1177/27.10.512319.
85. Rubio, F.J., Li, X., Liu, Q.R., Cimbro, R., and Hope, B.T. (2016). Fluorescence activated cell sorting (FACS) and gene expression analysis of Fos-expressing neurons from fresh and frozen rat brain tissue. J. Vis. Exp. *54358*. https://doi.org/10.3791/54358.
86. Braga-Lagache, S., Buchs, N., Iacovache, M.I., Zuber, B., Jackson, C.B., and Heller, M. (2016). Robust label-free, quantitative profiling of circulating plasma microparticle (MP) associated proteins. Mol. Cell. Proteomics *15*, 3640–3652. https://doi.org/10.1074/mcp.M116.060491.
87. Cox, J., and Mann, M. (2008). MaxQuant enables high peptide identification rates, individualized p.p.b.-range mass accuracies and proteome-wide protein quantification. Nat. Biotechnol. *26*, 1367–1372. https://doi.org/10.1038/nbt.1511.
88. UniProt Consortium (2019). UniProt: a worldwide hub of protein knowledge. Nucleic Acids Res. *47*, D506–D515. https://doi.org/10.1093/nar/gky1049.
89. Silva, J.C., Gorenstein, M.V., Li, G.Z., Vissers, J.P.C., and Geromanos, S.J. (2006). Absolute quantification of proteins by LCMSE: a virtue of parallel MS acquisition. Mol. Cell. Proteomics *5*, 144–156. https://doi.org/10.1074/mcp.M500230-MCP200.
90. Huber, W., von Heydebreck, A., Sültmann, H., Poustka, A., and Vingron, M. (2002). Variance stabilization applied to microarray data calibration and to the quantification of differential expression. Bioinformatics *18* (*Suppl 1*), S96–S104. https://doi.org/10.1093/bioinformatics/18.suppl_1.S96.
91. Kammers, K., Cole, R.N., Tiengwe, C., and Ruczinski, I. (2015). Detecting significant changes in protein abundance. EuPA Open Proteom. *7*, 11–19. https://doi.org/10.1016/j.euprot.2015.02.002.
92. Benjamini, Y., and Hochberg, Y. (1995). Controlling the false discovery rate: a practical and powerful approach to multiple testing. J. R. Stat. Soc. B Methodol. *57*, 289–300. https://doi.org/10.1111/j.2517-6161.1995.tb02031.x.
93. Liebscher, S., Keller, G.B., Goltstein, P.M., Bonhoeffer, T., and Hübener, M. (2016). Selective persistence of sensorimotor mismatch signals in visual cortex of behaving Alzheimer's disease mice. Curr. Biol. *26*, 956–964. https://doi.org/10.1016/j.cub.2016.01.070.
94. Scekic-Zahirovic, J., Sanjuan-Ruiz, I., Kan, V., Megat, S., De Rossi, P., Dieterlé, S., Cassel, R., Jamet, M., Kessler, P., Wiesner, D., et al. (2021). Cytoplasmic FUS triggers early behavioral alterations linked to cortical neuronal hyperactivity and inhibitory synaptic defects. Nat. Commun. *12*, 3028. https://doi.org/10.1038/s41467-021-23187-9.
95. Kato, S., Kaplan, H.S., Schrödel, T., Skora, S., Lindsay, T.H., Yemini, E., Lockery, S., and Zimmer, M. (2015). Global brain dynamics embed the motor command sequence of Caenorhabditis elegans. Cell *163*, 656–669. https://doi.org/10.1016/j.cell.2015.09.034.

STAR★METHODS

KEY RESOURCES TABLE

REAGENT or RESOURCE	SOURCE	IDENTIFIER
Antibodies		
Mouse anti parvalbumin	Swant	Cat#235; RRID: AB_10000343
Goat anti parvalbumin	Swant	Cat#PVG214; RRID: AB_10000345
Mouse anti calbindin	Abcam	Cat#ab82812; RRID: AB_1658451
Rabbit anti calbindin	Abcam	Cat#ab108404; RRID: AB_10861236
Rabbit anti-pCaMKII-α	Santa cruz	Cat#sc-12886-R; RRID: AB_2067915
Rabbit anti-CaMKII-α	Lifespan Bio	Cat#1178-50; RRID: AB_968870
Goat anti mCherry	Origene	Cat#AB0081; RRID: AB_2333094
Rabbit polyclonal anti mCherry	Abcam	Cat#ab183628; RRID: AB_2650480
Rabbit anti VGluT1	SYSY	Cat#135303; RRID: AB_887875
Rabbit anti VGAT	SYSY	Cat#131003; RRID: AB_887869
Rabbit anti HOMER-3	Origene	Cat#TA308627
Rabbit anti HOMER-3	SYSY	Cat#160303; RRID: AB_10804288
Mouse anti GFP	ABCAM	Cat#AB1218; RRID: AB_298911
Mouse anti myc	Cell signaling	Cat# 2276; RRID: AB_331783
Mouse anti Frrs1l	Santa cruz	Cat# sc-398692
Mouse anti GluR2	Millipore	Cat#MAB397; RRID: AB_11212990
Chicken anti MAP2	Sigma/Millipore	Cat#AB15452; RRID: AB_805385
rabbit anti GABA	Sigma	Cat#A2052; RRID: AB_477652
Rabbit anti KV1.2	Thermo Fisher Scientific	Cat# PA5-77578; RRID: AB_2736054
Rabbit anti-GFAP	Sigma	Cat#G4546; RRID: AB_1840895
Rabbit anti-SORCS3	Novus	Cat##NBP1-30615; RRID: AB_2192266
Donkey anti-Goat IgG (H+L) Cross-Adsorbed Secondary Antibody, Alexa Fluor™ 594	Invitrogen, Thermo Fisher Scientific	Catalog # A-11058
Neurotrace 435/455 blue fluorescent Nissl stain	Invitrogen, Thermo Fisher Scientific	Catalog number: N21479
Bacterial and virus strains		
AAV2/1-hSyn-GCaMP7S-WPRE	Dana et al.[20]	Addgene: 104487-AAV1
AAV2/1-hSyn-DIO-mCherry	Unpublished, a gift from Bryan Roth to Addgene	Addgene: 50459-AAV1
AAV2/2-hSyn-DIO-mCherry	Unpublished, a gift from Bryan Roth to Addgene	Addgene: 50459-AAV2
AAV2/8-hSyn-DIO-mCherry	Unpublished, a gift from Bryan Roth to Addgene	Addgene: 50459-AAV8
AAV2/8-hSyn-DIO-hM3D(Gq)-mCherry	Krashes et al.[77]	Addgene: 44361-AAV8
AAV2/8-hSyn-DIO-hM4D(Gi)-mCherry	Krashes et al.[77]	Addgene: 44362-AAV8
AAV2/2-hSyn-DIO-hM4D(Gi)-mCherry	Unpublished, a gift from Bryan Roth to Addgene	Addgene: 50475-AAV2
AAV2/1-hSyn-GCaMP6s-WPRE-SV40	Chen et al.[19]	Addgene: 100843-AAV1
AAV2/1-Syn-NES-jRCaMP1a-WPRE-SV40	Dana et al.[78]	Addgene: 100848-AAV1
AAV2/1-hSyn-Twitch2B-WPRE-SV40	Thestrup et al.[23]	Addgene: 100040- AAV1

(*Continued on next page*)

Continued

REAGENT or RESOURCE	SOURCE	IDENTIFIER
C9orf4 (FRRS1L) - Human shRNA lentiviral particles		Origene: CAT# TL314264V
C9ORF4 (FRRS1L) - Human Myc-DDK-tagged lentiviral particles		Origene: CAT#: RC221300L1V
Chemicals, peptides, and recombinant proteins		
SB 431542	Stem cell technologies	Cat#72234
LDN193189	Stem cell technologies	Cat#72147
CHIR99021	Stem cell technologies	Cat#72052
L-Ascorbic Acid	Sigma Aldrich	Cat#A4403
SAG	Stem cell technologies	Cat#73412
BDNF	Stem cell technologies	Cat#78005
DAPT	Stem cell technologies	Cat#72082
GDNF	Stem cell technologies	Cat#78058
IGF-1	Stem cell technologies	Cat#78078
CNTF	Stem cell technologies	Cat#78010
Clozapine N-Oxide	Tocris	Cat#4936
Experimental models: Cell lines		
Human induced pluripotent stem cell (SCA1)	Buijsen et al.[38]	LUMCi002
Human induced pluripotent stem cell (Healthy)	Buijsen et al.[38]	LUMCi003
Human induced pluripotent stem cell (SCA1)	Leiden University Medical Center	LUMCi034
Human induced pluripotent stem cell (Healthy)	Leiden University Medical Center	LUMCi035
Human induced pluripotent stem cell (SCA1)	Leiden University Medical Center	LUMCi022
Human induced pluripotent stem cell (Healthy)	Leiden University Medical Center	LUMCi023
Experimental models: Organisms/strains		
B6.129S-Atxn1^{tm1Hzo}/J	Jackson laboratories	RRID: IMSR_JAX:005601
B6;129P2-$^{Pvalbtm1(cre)Arbr}$/J	Jackson laboratories	RRID: IMSR_JAX:008069
B6.129-Tg(Pcp2-cre)2Mpin/J	Jackson laboratories	RRID: IMSR_JAX:004146
Software and algorithms		
Fiji	https://doi.org/10.1038/nmeth.2019	RRID:SCR_002285
Imaris	Oxford instruments	RRID:SCR_007370
iMOD	Kremer et al.[79]	RRID:SCR_003297
Graphpad prism	http://www.graphpad.com/	RRID:SCR_002798
MATLAB R2018a version	The MathWorks, Inc https://de.mathworks.com/	RRID:SCR_001622
Custom built software on Labview 2018 SP1, 2020 SP1, National Instruments	Keller et al.[80] National Instruments	https://www.ni.com/de-de/shop/software/products/labview.html
SciScan 1.4 - Imaging acquisition software	Scientfica UK	N/A
Other		
IR camera	Imaging source	DMK 22BUC03
Ti:Sapphire laser with a DeepSee pre-chirp unit	Spectra Physics MaiTai HP	N/A
Two-photon microscope, equipped with an 8 kHz resonant scanner	Hyperscope, Scientifica	N/A
×16 water-immersion objective (0.8 NA)	Nikon	N/A

(*Continued on next page*)

Continued

REAGENT or RESOURCE	SOURCE	IDENTIFIER
PMT	FEMTO	DHPCA-100
Emission filter		G 525/50 nm, C/Y 460/80nm (CFP) and 560/80 nm (YFP)

RESOURCE AVAILABILITY

Lead contact

Further information and requests for resources and reagents should be directed to and will be fulfilled by the lead contact, Smita Saxena (smita.saxena@dbmr.unibe.ch).

Materials availability

This study did not generate new unique reagents.

Data and code availability

- All data reported in this paper will be shared by the lead contact upon request.
- This paper does not report original code.
- Any additional information required to reanalyze the data reported in this paper is available from the lead contact upon request.

EXPERIMENTAL MODEL AND SUBJECT DETAILS

Mice strains

The *Atxn1*$^{154Q/2Q}$ knock-in mice (B6.129S-Atxn1tm1Hzo/J),[81] called *Sca1* throughout the manuscript, *PV-IRES- cre* mice (B6;129P2-Pvalbtm1(cre)Arbr/J) and *Pcp2-cre* (B6.129-Tg(Pcp2-cre)2Mpin/J) were obtained from Jackson Laboratory. To obtain *Sca1::PV or Sca1::Pcp2* animals, *Atxn1*$^{154Q/2Q}$ males were crossed with *PV-cre* or *Pcp2-cre* homozygous females. Animals of both genders were equally used in the study. Mice were kept at a 12/12-hour light/dark cycle with ad libitum access to food and water and were group housed. We regularly performed long-range PCR on *Sca1* mice, confirming the length of PolyQ repeats in both colonies as being around 154 repeats. Animal care, housing, ethical usage, and procedures were approved by the government of upper Bavaria and in accordance with the Swiss Veterinary Law guidelines.

METHOD DETAILS

Pharmacological treatments

Clozapine-N-oxide (Tocris, 4936) was administered IP at a dosage of 3 mg/Kg, 45 minutes prior to behavioral test (for acute MLIN modulation) or in drinking water 40 μg/ml[82] for chronic modulation of MLIN expressing the inhibitory G protein hM4D(Gi) or hM3D(Gq). All CNO treatments were independently performed at UBERN and LMU.

Accelerating Rotarod

Rotarod test was performed between 1 pm and 6 pm. Experimental mice were habituated to the experimenter and trained on the rotating rod at fixed speed of 5 rpm for three days prior to the first rotarod recording. The protocol consisted of 4 trials per day, in which the rotating rod accelerated from 5 to 40 rpm within 300s, followed by 300s rest in between trials. To avoid experimenter bias, rotarod for chronic DREADD(Gi) experiments were performed independently both at the LMU and UBERN. Experimenters were blinded for treatment condition throughout the study and data was merged and presented together.

Hindlimb clasping assay

The tails of the mice were grabbed at the base and mice were lifted for 20 seconds. If both hind limbs were consistently splayed outward, away from the abdomen it was assigned a score of ''0''. If only one of the hindlimbs was retracted near the abdomen for the majority of the time, the score assigned was ''1''. If both hindlimbs are retracted close to the abdomen, the animal receives a score of ''2''. Finally, if both hindlimbs were tightly clinched to the abdomen the score assigned was ''3''. Clasping phenotype for chronic DREADD(Gi) experiments was measured independently at the LMU and UBERN, data was merged and presented together.

DREADDs and genetically encoded calcium indicators for *in vivo* imaging

Cre dependent DREADDs and genetically encoded calcium indicators were purchased from Addgene: AAV2/1-hSyn-DIO-mCherry (50459) viral titer 7×10^{12} vg/mL, AAV2/2-hSyn-DIO-mCherry (50459) viral titer 4×10^{12} vg/mL, AAV2/8-hSyn-DIO-mCherry

(50459) viral titer 1×10^{13} vg/mL, AAV2/8-hSyn-DIO-hM4D(Gi)–mCherry (44362) viral titer 1×10^{13} vg/mL, AAV2/8-hSyn-DIO-hM3D(Gq)–mCherry (44361) viral titer 4×10^{12} vg/mL and AAV2/8-hSyn-DIO-hM4D(Gi)–mCherry (50475) 7×10^{12} vg/mL. For calcium imaging: AAV2/1-hSyn-GCaMP6s-WPRE-SV40 (100843) viral titer 1×10^{13} vg/mL; AAV2/1-hSyn-jGCaMP7s-WPRE (104487) viral titer 1×10^{13} vg/mL. AAV2/1-hSyn1-Twitch2B-WPRE.SV40 (100040) viral titer 1×10^{13} vg/mL.

Intracerebroventricular (i.c.v.) injection

Injection of AAV particles in neonates (P0-P2) was performed by unilateral injection of 1.0 μl of AAV2/8-hSyn-DIO-hM4D(Gi)–mCherry. The viral particles were injected in the left lateral ventricle, as described previously.[83] A 0.1% fast green solution was added to the vector suspension, in order to visualize the spread of the virus.

Surgical procedures in adult animals at UBERN

To induce analgesia, animals were injected IP with 0.1 mg/kg Buprenorphine 20 minutes prior to the surgical procedure. Anesthesia was induced using an induction chamber with 5% isoflurane, animals were then placed onto the stereotaxic frame and anesthesia was maintained at 1.5-2% isoflurane throughout the surgical procedure. Body temperature was maintained using a heating pad, and a lubricating eye cream was applied to avoid dehydration of the corneas. The head of the animal was fixed with ear bars. Under a dissecting microscope (Olympus, Tokyo, Japan) a medial skin incision was performed to expose the skull, the incision was extended in order to expose bregma and lambda to align the skull. In order to expose the occipital part of the cerebellum, muscles were cut over the medial line and muscles fibers were gently opened to access the injection site. A drill was used to make two holes in the occipital bone. For DREADDs-mediated circuit modulation experiments, the following coordinates were used to inject AAV2/8-hSyn-DIO-hM4D(Gi)–mCherry, AAV2/8-hSyn-DIO-hM3D(Gq)–mCherry and AAV2/8- hSyn-DIO-mCherry: AP -8.25mm, DV -2.5mm, ML +/- 1mm, angle 57 °, depth 0.3-0.4 mm from the dura. For the FACS sorting of MLIN the following coordinates were used: AP - 8.25mm, DV -2.5mm, ML 0 and /+/-1 mm, angle 57 °, depth 0.3-0.4 mm from the dura; AP -7.25mm, DV -1 mm, ML 0 and /+/-1.5 mm, angle 0 °, depth 0.3-0.4 mm from the dura. A Hamilton syringe equipped with a glass pipette was used to infuse 300nl (or 500nl for FACS sorting) of virus per injection site at an infusion rate of 50nl/minute. After the completion of the injection, the glass pipette was left in place for few minutes before withdrawal. Following the glass pipette withdrawal, the muscles and the skin were sutured. A subcutaneous injection of warm saline was applied, and animals were placed in a pre-warmed cage and monitored until fully awake and recovered from the anesthesia.

Cranial window implantation and virus injection at LMU

Mice of both sexes were implanted with a cranial window at P42 ± 6.70 (mean ± SD, P60 cohort) for imaging early symptomatic mice and at P174 ± 2.91 for late symptomatic mice (P200 cohort). They received a stereotaxic injection of AAV2/1-hSyn-jGCaMP7s-WPRE, diluted 1:10 in saline, Addgene viral prep # 104487-AAV1; RRID: Addgene_104487-AAV1 into lobule V (5Cb) & VI (6Cb) of the cerebellar vermis. Mice were given Meloxicam (10 mg/kg) and Metamizol (200 mg/kg) 30 minutes prior to surgery, orally and were then anesthetized with Fentanyl (0.05 mg/kg), Midazolam (5.0 mg/kg), and Metedomidin (0.5 mg/kg) given intraperitoneally. A circular craniotomy of 3 mm diameter was centered at 1.5 mm lateral from the midline and -6.5 mm posterior to bregma overlying lobule V & VI and injections were made at two sites at -6.5mm anterior/posterior (AP) and 0.5 mm lateral and -6.8 mm AP and 1mm lateral from the midline (Figure 1B), with 200nl AAV injected at a depth of both 500μm and 150μm from the cortical surface at each site, using a flow rate of 50nl/min. A 3 mm round glass coverslip (Warner Instruments) was placed over the craniotomy and sealed flush to the surrounding skull using UV-curable dental acrylic (Venus Diamond Flow, Heraeus Kulzer GmbH). To allow head fixation during two-photon imaging, a custom metal head bar was then attached onto the skull using dental acrylic (Paladur, Heraeus Kulzer GmbH). At the end of the procedure the anesthesia was antagonized through application of Atipamezol (2.5 mg/kg), Flumazenil (0.5 mg/kg) und Naloxon (1.2 mg/kg, all i.p.) and Meloxicam (10 mg/kg) was then administered orally at 12, 24, 36-, 48-, 60- and 72-hours post-op.

Two-photon imaging in awake and anesthetized mice

Early symptomatic mice were imaged at P63 ± 3.85 (mean ± SD), and late symptomatic mice at P204 ± 3.60. To habituate the mice, each was given a minimum of three training sessions of 20 minutes each across the 7 days prior to first imaging time point, allowing them to become comfortable running head restricted on the air-supported treadmill and engaging with the virtual reality environment. *In vivo* two-photon imaging was performed using a two-photon microscope (Hyperscope, Scientifica, equipped with an 8 kHz resonant scanner) at a frame rate of 30 Hz and a resolution of 512 × 512 pixels. Light source was a Ti:Sapphire laser with a DeepSee prechirp unit (Spectra Physics MaiTai eHP). GCaMP7s was excited at 910 nm, with a laser power around 30–70 mW and emitted photons detected by a GaAsP PMT with a bandpass filter in front (525/50 nm). Using a 16x water-immersion objective (Nikon), stacks consisting of 15,000 frames (equivalent to ~8 min) were acquired covering a field of view (FOV) of 453 x 453μm to simultaneously image molecular layer interneurons, Purkinje neurons and Golgi cells. Two-three FOVs at this resolution were imaged per mouse, each under three distinct conditions, (1) in a virtual reality environment depicting a linear track with patterned walls consisting of lines and dots of contrasting colour, providing visual feedback for locomotion (fb), (2) in darkness (dark), and (3) under light isoflurane anesthesia (iso).

Mice were anesthetized with isoflurane initially at a volume of 2-2.5 Vol % in pure O_2 at a flow rate of 0.5 l/min. This was gradually reduced to 1.0-1.5 Vol % over a minimum of 30 minutes induction period in order to establish a respiratory rate of between 110-130

breaths per minute, which was then maintained throughout the recording. A physiological monitoring system (Harvard Apparatus) was used to ensure body temperature was stable at 37 degrees. Several behavioral parameters were recorded synchronized with the imaging data acquisition. As such the speed of the mouse on the ball was tracked by an optical mouse sensor (Logitech G500s Laser Gaming Mouse) placed in front of the styrofoam ball. Pupil position and width as well as whisking events were detected in video recordings acquired with an infrared camera (The Imaging Source, DMK 22BUC03, USB 2.0 monochrome industrial camera), positioned to the front right of the mouse to visualize the right eye and whiskers on this side. Information of pupil position and pupil width were derived online using custom-build software (National Instruments). Pupil width was computed post hoc using a custom-written script (Math Works). Whisking was tracked by superimposing a detection window over mouse's snout area. Brief puffs of pressurized air were applied through a thin tube positioned at the right side of the mouse's body.

Ratiometric calcium imaging

A circular craniotomy was performed at 3 mm diameter, centered at 1.5 mm lateral from the midline and -6.5 mm posterior to bregma on mice aged P42 (± 7.27). Overall surgical procedure is as described above. Stereotaxic injections of AAV2/1-hSyn-Twitch-2B-WPRE (containing the two fluorescent proteins mCerulean3 and cpVenusCD as a FRET pair) at two sites of -6.5mm anterior/posterior (AP) and 0.5 mm lateral and -6.8 AP and 1mm lateral from the midline, with 200nl AAV injected at a depth of both 500μm and 150μm from the cortical surface at each site (50nl/min, diluted 1:3 in saline). The following recovery time and habituation for imaging experiments was consistent as initially described above. Twitch-2B was excited at 860 nm, with a laser power around 30-70 mW, emitted photons were detected via two PMTs (passing through bandpass filters: 460/80nm (CFP) and 560/80 nm (YFP)) using identical voltage settings (800 for the blue channel, 830 for the yellow channel) for all animals. Stacks consisted of 15,000 frames and were acquired with a FOV of 453 x 453μm to simultaneously image molecular layer interneurons, Purkinje neurons and Golgi cells. Imaging conditions used were darkness and subsequent isoflurane anesthesia, as described above. Imaging experiments were conducted at ages P73 (± 8.20).

Imaging data was processed in a similar fashion as the GCaMP7s recordings, including motion correction and semimanual segmentation to identify regions of interest. The calcium trace here corresponds to the ratio between the yellow channel and the cyan channel (Y/C ratio).

Chronic CNO treatment at LMU-UBERN

To investigate the effects of chronic MLIN inhibition/activation, we either injected inhibitory or excitatory DREADD or control mCherry AAV, diluted 1:6 in saline into the cerebellar vermis at the age of P40-45. For induction of anesthesia and application of analgesics, the surgery protocol was as described for imaging experiments. Two small holes (approximately 300μm diameter) were drilled on either side of the midline to allow injection via micropipette at the following coordinates AP -8.25mm, DV 2.5, ML +/-1mm. Injections were made at a 57° angle to a 0.3-0.4 depth from touching the dura surface (rate 50nl/min). Clozapine-n-oxide (CNO, 40μg/ml) was administered through the drinking water with 1% sucrose, to mask the CNO taste. Mice were given 1% sucrose water 3 days prior to start of treatment to get used to the taste, every 3 days throughout the treatment CNO solution was prepared fresh, mice were weighed and assessed for any physical impairments. Rotarod (as described above/5-40 RPM, 300 seconds) was performed prior to treatment start, with 4 trials (300 second intervals) over 3 days, then 4 trials on 2 consecutive days as depicted in main figure schemes. Handling of mice (minimum twice per week) and habituation around rotarod (minimum once per week) was performed regularly throughout.

Calcium imaging with acute CNO administration

All surgical procedures were performed as described above in WT*::PV* mice and *Sca1::PV* mice at P73 (± 4.46). A circular craniotomy of 3 mm diameter, centered at 1.5 mm lateral from the midline and -6.5 mm posterior to bregma was drilled. Injections of AAV2/1-hSyn-GCaMP7s-WPRE were then made at two sites of -6.5mm anterior/posterior (AP) and 0.5 mm lateral and -6.8 mm AP and 1mm lateral from the midline, with 200nl AAV injected at a depth of both 500μm and 150μm from the cortical surface at each site (50nl/min, diluted 1:10 in saline). Injections of AAV2/8-hSyn-DIO-hM4Gi-WPRE were also made, bilaterally at -6.8 AP, +/-1mm from the midline, 150μm from the cortical surface at each site. And again, bilaterally at AP -8.25mm, DV 2.5, ML +/-1mm. The latter two injections at AP -8.25mm were made at a 57° angle to a 0.3-0.4 mm depth from touching the dura surface (50nl/min, diluted 1:3 in saline).

Mice were then imaged at P110 (± 5.26) (habituation protocol as described above) and then the same neurons were again imaged at P114 (± 4.47) 45 minutes following an intraperitoneal injection of clozapine-N-oxide (CNO, 3mk/kg). Mice were imaged as described above, using the same imaging equipment, however we only assessed neuronal activity during feedback as well as under isoflurane anesthesia (isoflurane 1.0-1.5 Vol % at a flow rate of 0.5 l/min to establish respiratory rates between 110-130 breaths per minute, induction process and physiological monitoring as described in initial two photon imaging experiments).

For control acute CNO experiments without injection of DREADDs, *Sca1* mice at age P80 underwent the exact same surgical procedures with viral injections AAV2/1-hSyn-GCaMP7s-WPRE and AAV2/8-hSyn-mCherry. The mice were then imaged at P120 and P121 for baseline and CNO experiments respectively following procedures and conditions as the DREADDs mice.

Immunofluorescence of rodent tissue at UBERN

Mice were transcardially perfused with 4% paraformaldehyde (PFA) in 1X PBS at UBERN, while in LMU animals were transcardially perfused with 1x PBS 0.05% Heparin, followed by 4% PFA; the cerebellum was isolated and kept overnight at 4°C in

the same fixative solution, followed by 30% sucrose in PBS for cryoprotection until samples were used. After embedding in Tissue Tek O.C.T compound (Bio system, 4583), cerebellar sections (50 μm) were sagitally sliced while brain was sliced coronally (50 μm) using a cryostat. Antibodies used for immunofluorescence were: mouse anti-Parvalbumin (1:1000, Swant, 235), goat anti-Parvalbumin (1:1000, Swant, PVG213), mouse anti-Calbindin (1:1000, Abcam, ab82812), rabbit anti-Calbindin (1:1000, Abcam, ab108404), rabbit anti-pCaMKII-α, (1:200, Santa cruz, sc-12886), rabbit anti-CaMKII-α, 1:500 (LSB1178, Lifespan Bio), goat anti-mCherry (1:1000, Origene, AB0081-200), rabbit anti-mCherry (1:1000, Abcam, ab183628), rabbit anti-VGluT1 (1:1000, SYSY, 135303), rabbit anti-VGAT (1:1000, SYSY, 131003), rabbit anti-Homer-3 (1:500, Origine, TA308627), rabbit anti-Homer-3 (1:1000, SYSY, 160303) mouse anti-Frrs1l (1:100, Santa cruz, sc-398692), mouse anti-GluR2 (1:500, Millipore, MAB397). Sections were kept for 2h in PBS solution containing 0.05% Triton X-100 and 10% normal donkey serum (NDS, Jackson immunoresearch, 017-000-121), after the antibodies were applied in PBS, 3% NDS, 0.05% Triton X-100, and incubated overnight at 4°C. Sections were then briefly washed with PBS and incubated for 120 min at room temperature (RT), with appropriate combinations of secondary antibodies from Invitrogen.

Confocal microscopy

Confocal images were acquired using an Olympus Fluoview 1000-BX61 (Olympus, Tokyo) microscope, fitted with a 20X, 40X air objective or 60X immersion oil objective. For the analysis of intensities, data were acquired using identical confocal settings, with signals at the brightest cells being non-saturated.

SBF-SEM

Anesthetized mice were transcardially perfused first with 0.1 M PBS (pH=7.4) and then fixed with fixation solution (2.5% glutaraldehyde (GA) +2% PFA in 0.1 M Na-cacodylate, pH=7.4). Cerebellum was isolated and post-fixed in fixation solution. Bloc staining, dehydration and embedding were performed as follows: post-fixation in 0.15 M cacodylate buffer, 1.5% potassium ferrocyanide and 2% osmium tetroxide, followed by sample incubation with 0.64 M pyrogallol for 15min at room temperature and for 5min in a water bath at 50 °C, and subsequently rinsed with water. Samples were incubated in 2% OsO4 for 22min at room temperature and 8min in a water bath at 50°C. After water rinses, the samples were incubated overnight in a solution of 0.15 M gadolinium acetate (LFG Distribution, Lyon, France) and 0.15 M samarium acetate (LFG Distribution) pH 7.0. Followed by water rinses, samples were incubated in 1% Walton's lead aspartate,[84] particularly useful for ultra-structural enzymology12 at 60°C for 30min. After staining, the samples were dehydrated in a graded ethanol series (20%, 50%, 70%, 90%, 100%, 100%) at 4°C, each step last for 5min. The blocks were infiltrated with Durcupan resin mixed with ethanol at ratios of 1:3 (v/v), 1:1, and 3:1, each step lasted for 2h, to finally be infiltrated with pure Durcupan overnight. The samples were transferred to fresh Durcupan and the resin was polymerized for 3 days at 60°C. Care was taken to have osmicated material directly exposed at the block surface in contact with the glue in order to reduce specimen charging under the electron beam. Pyramids with a surface of approximately 500 × 500 μm2 were trimmed with a razor blade. The blocs were imaged at the SBF-SEM using a Quanta FEG 250 (FEI, Eindhoven, The Netherlands), equipped with a 3View2XP in-situ ultramicrotome (Gatan). Images were acquired in low or high vacuum according to block quality. Analysis was performed using Fiji, were axosomatic synapses were counted within different PNs soma. For 3D representative images iMOD software was used and PN, MLIN and synapses were manually ROI to reconstruct the final model (around 100 and 280 consecutive images were used for WT and *Sca1* models).

iPSC differentiation into GABAergic neurons (iGNs)

The *Control* and *SCA1* iPSCs were obtained from Dr. Ronald A.M. Buijsen, and Dr. Willeke M.C. van Roon-Mom. Leiden University Medical Center (LUMC), Leiden, The Netherlands. iPSCs were cultured in GeltrexTM (ThermoFischer) coated plates in mTeSRTM1 (StemCell technologies) media. Briefly, human iPSCs were dissociated to single cells using Accutase (StemCell technologies) and seeded at $3X10^6$ onto 10 cm plate with N2B27 differentiation medium (Advanced (DMEM/F12), Neurobasal (1:1) medium, 1% Pen/strep (Gibco), 1% GlutaMAX (Gibco), 0.1mM 2- mercaptoethanol (Gibco), 1X B27 supplement (Gibco), 1X N2 supplement (Gibco), supplemented with 10ng/ml basic fibroblast growth factor ((StemCell technologies), 20 μM SB431542 (StemCell technologies), 0.1 μM LDN193189 (StemCell technologies), 3 μM CHIR99021 (StemCell technologies), 10 μM L-Ascorbic Acid (L-AA; Sigma) and 1X Revitacell supplement (Gibco)) to initiate the formation of embryoid bodies (EBs). On day 2, media patterning of EBs was induced by the addition of media supplemented with 500 nM Smoothened Agonist (SAG; StemCell technologies). EBs were pelleted and fed with fresh media on every alternate day until day 14. 10 ng/ml Brain derived neurotrophic factor (BDNF; StemCell technologies) was added from day 7 while 10 μM DAPT (StemCell technologies) was added from day 9. EBs were dissociated using trypsin on day 16 and triturated with ice cold cell trituration and wash medium (1X PBS (Gibco), 0.45% Glucose, 0.1% Bovine Serum Albumin (BSA; Sigma), 2mM MgCl2, 0.8mM EDTA (Invitrogen), 2.5% Fetal Bovine Serum (FBS; Sigma), 1X N2 supplement, 1X B27 supplement and DNAse). Triturated EBs were then plated on poly-ornithine/laminin (Sigma) coated plates in iGNs feeding medium (Neurobasal medium (Gibco), 1X glutaMAX, 1X Non-essential amino acid (NEAA, Gibco), 0.1mM 2- mercapthoethanol, 1X N2 supplement, 1X Pen/strep, 1X B27 supplement, 10ng/ml glial cell derived neurotrophic factor (GDNF; StemCell technologies), BDNF 10ng/ml, 10ng/ml insulin- like growth factor (IGF-1; StemCell technologies), 10ng/ml Ciliary neurotrophic factor (CNTF; StemCell technologies) and 10 μM AA and kept at incubator at 37°C and 5% CO2 for further maturation up to two weeks.

Immunofluorescence staining of iGNs

iGNs plated on coverslips were fixed using 4% PFA for 15min and blocked for 1h with 3% bovine serum albumin (BSA) and 0.1 % TritonX-100 in phosphate buffered saline PBS. After blocking, neurons were incubated with the following primary antibodies: mouse anti- Parvalbumin (1:1000, Swant, 235), goat anti-Parvalbumin (1:1000, Swant, PVG213), chicken anti-MAP2 (1:1000, Sigma, AB15452), rabbit anti-GABA (1:500, Sigma, A2052), mouse anti- GFAP (1:500, Sigma, G4546), mouse anti-Frrs1l (1:100, Santa cruz, sc-398692), mouse anti- GluR2 (1:500, Millipore, MAB397), mouse anti-myc (1:1000, Cell Signaling, 2276), mouse anti-GFP (1:1000, ABCAM, AB1218), rabbit anti-SORCS3 (1:500, Novus biologicals, NBP1-30615) in blocking buffer overnight at 4°C. After washing three times with PBS, cells were incubated in blocking buffer with Alexa Fluor fluorescently labeled secondary antibodies and DAPI for 1h at room temperature. Cells were then washed with PBS and mounted on glass slides. Images were acquired with a confocal microscope Olympus FluoViewTM FV1000 (Olympus) fitted with a 20X or 40x air objective and 60x immersion oil objective.

FACS of MLIN

Protocol for isolation of MLIN from adult animals was performed as in Rubio et al.,[85] with some optimization. Animals were deeply anesthetized with isoflurane and decapitated, the cerebellum was extracted and placed on an ice-cold petri dish. A drop of Hibernate A media (Gibco), supplemented with 1X B27 (Gibco) was used to cover the fresh cerebellum and a razor blade was used to mince the tissue. The tissue was then centrifuged at 110x g for two minutes at 4°. The supernatant was discarded and 1 ml of Accutase was added to resuspend the pellet. Tubes were incubated at 4°C for 30 minutes with hand-over-end mixing followed by centrifugation at 960x g for 2 minutes at 4°C. Supernatant was discarded and pellet resuspended in 0.6 ml of Hibernate A + B27 media. Single cells were obtained by mechanical trituration using a glass pipette. Samples were triturated 10 times and let settle in ice to collect the supernatant and the pellet was resuspended again in 0.6ml of Hibernate A + B27 media. The procedure was repeated until ~ 3 ml of supernatant was collected. The collected supernatant was then filtered through 100 and 40 μm cell strainer and 2 additional ml of Hibernate A + B27 media were added to the filtered supernatant. Hoechst was added to the single cell suspension and double positive neurons for mCherry and Hoechst were sorted using MoFlo ASTRIOS EQ (Beckman Coulter) in 300 μl of sterile DPBS. Samples were centrifuged at 400x g for 15 minutes and ~ 250 μl of DPBS was discarded and sorted cells in approximately 50 μL DPBS were frozen, then lyophilized, and stored at -80C until further use.

Mass spectrometry of sorted MLIN

The lyophilizate was re-suspended in 10 μL 8M Urea / 100mM Tris-HCl pH8, containing proteases inhibitor cocktail (Complete EDTA free, Roche, Rotkreuz), reduced, alkylated and digested with additions of 100 ng, each, of LysC for 2 hours at 37°C followed by Trypsin (both sequencing grade from Promega) at room temperature overnight as described by Braga-Lagache et al.[86] The digests were analyzed by nano-liquid chromatography on a Dionex, Ultimate 3000, (ThermoFischer Scientific, Reinach, Switzerland) coupled to a timsTOF Pro (Bruker Daltonics, Bremen, Germany), through a CaptiveSpray source (Bruker, Bremen, Germany) with an end-plate offset of 500 V, a drying temperature of 200 °C, and with the capillary voltage fixed at 1.6 kV. A volume of 2 μL from the protein digest were loaded onto a pre-column (C18 PepMap 100, 5 μm, 100A, 300 μm i.d. x 5mm length, ThermoFisher) at a flow rate of 10 μL/min with 0.05% TFA in water/acetonitrile 98:2. After loading, peptides were eluted in back flush mode onto a homemade C18 CSH Waters column (1.7 μm, 130 Å, 75 μm × 20 cm) by applying a 90-minute gradient of 5% acetonitrile to 40% in water / 0.1% formic acid, at a flow rate of 250 nl/min. The timsTOF Pro was operated in the Parallel Acquisition Serial Fragmentation (PASEF) mode. The mass range was set between 100 and 1700 m/z, with 10 PASEF scans between 0.6 and 1.6 V s/cm2. The accumulation time was set to 2 ms, and the ramp time was set to 100 ms. Fragmentation was triggered at 20,000 arbitrary units (au), and peptides (up to charge 5) were fragmented using collision induced dissociation with a spread between 20 and 59 eV.

Calcium imaging of iGNs and lentiviral-mediated FRRS1l transduction

iGNs were transduced with constitutive AAV2/1-Syn-GCaMP6s-WPRE-SV40 at DIV5, and imaging was performed on DIV12 using an Olympus Fluoview 1000-BX61 (Olympus, Tokyo) microscope fitted with a 40X water immersion objective. For FRRS1l overexpression, iGNs were transduced at DIV4 with lentiviruses LV::*FRRS1L*-myc (Origene, RC221300L1V) and at DIV7 with AAV2/1-Syn-GCaMP6s-WPRE-SV40. For the knockdown of FRRS1L, iGNs were transduced at DIV4 with LV::sh*FRRS1L*-GFP (Origene, TL314264V) and subsequently transduced with AAV2/1-Syn-NES-jRCaMP1a-WPRE-SV40. Calcium imaging was performed at DIV12-14. Cells were incubated in the recording solution containing 115mM NaCl, 5.6mM KCl, 1mM NaH2PO4, 2 mM CaCl2, 1mM MgCl2, 11mM glucose and 25mM NaHCO3 for 10 minutes before imaging. Images were acquired every 10 seconds, the first 40 seconds were considered as baseline, afterwards 50mM KCl was added to the imaging solution to depolarize the cells. All experiments were performed from three-five independent culture differentiations/line. Images were analysed using Fiji, neuronal somata were assessed as ROIs and median intensity over time was measured. To calculate ΔF, the median intensity values are divided by the average of the first 40 seconds of recording (F0) per single ROI.

QUANTIFICATION AND STATISTICAL ANALYSIS

Microscopy and image analysis

For parvalbumin, P-CaMKII, CaMKII, Calbindin, Frrs1l, signal intensity values were calculated over a maximal intensity projection of several consecutive Z-stack spaced 0.5 μm. Cells were manually ROI and average intensity was measured with Fiji. For parvalbumin

and Frrs1l, neurons with values of intensity below 50 arbitrary units (a.u.) were considered as low expressing, between 50 and 100 a.u. as medium expressing and above 100 a.u. as high expressing. Intensity values were plotted using GraphPad Prism 9. For GluR2 expression analysis, 5 random spots within the cellular membrane of PV positive MLIN were measured using Fiji, the average of the 5 points were plotted using GraphPad Prism 9. The spread of mCherry positive MLIN for chronic inhibition of cerebellar MLIN was counted in 8 mCherry and 9 DREADD(Gi) injected animals between UBERN and LMU, multiple areas within every image (total of 142 images, approximately 8-9 sections/animal) were used to analyze the number of positive MLIN, PN and GCL neurons.

For the analysis of VGAT and VGluT1 synapses 4 Z-stacks spaced 0.5 μm were used. Both neurons soma and synapses were reconstructed in 3D using Imaris software (version 7.6.3), only synapses in contact with the cell membrane were counted for density analysis. For Homer-3 synapses analysis 3 Z-stacks spaced 0.5 μm were used. Puncta were reconstructed in 3D using Imaris software within a ROI of 35.4 μm^2 and the number of synapses was plotted using GraphPad Prism 9.

Analysis of fluorescence intensity for iGNs SORCS3 signal intensity values were calculated over a maximal intensity projection of consecutive Z-stack spaced 0.5 μm, neurons with values of intensity up to 70 a.u. were considered as non-expressing SORCS3, and neurons with values above 70 a.u. were considered as expressing SORCS3. Background fluorescence intensity was between 20-50 a.u. For parvalbumin intensity analysis neurons were considered low expressing with values below 70 a.u., medium with values between 70 and 100 a.u. and high expressing with values over 100 a.u.

Data analysis of mass spectrometry

All samples were processed with MaxQuant[87] (version 2.0.1.0), with first and main peptide search tolerance set to 20, respectively 10 ppm, and MS/MS match tolerance to 40 ppm. MaxQuant's TIMS-DDA default instrument settings were kept. Enzyme specificity was set to strict trypsin, and a maximum of three missed cleavages were allowed. Carbamidomethylation on cysteine was set as a fixed modification, methionine oxidation and protein N-terminal acetylation as variable modifications. Sorted cell samples were searched against the manually reviewed uniprot.[88] Mus musculus database (release July 2020), subsequent mouse samples with the full uniprot database (release June 2021). Common contaminants were added in each case. Protein intensities are reported as MaxQuant's Label Free Quantification (LFQ) values, as well as iTop3[89] values (sum of the intensities of the three most intense peptides); for the latter, variance stabilization[90] was used for the peptide normalization, and missing peptide intensities, if at least 2 evidences exist in a group, were imputed by drawing values from a Gaussian distribution of width 0.3 centered at the sample distribution mean minus 2.8x the sample standard deviation. Imputation at protein level for both iTop3 and LFQ was performed if there were at least two measured intensities in at least one group of replicates; missing values in this case were drawn from a Gaussian distribution of width 0.3 centered at the sample distribution mean minus 2.5x the sample standard deviation. Differential expression tests were performed using empirical Bayes (moderated t-test) implemented in the R limma package.[91] The Benjamini and Hochberg[92] method was further applied to correct for multiple testing. The criterion for statistically significant differential expression is that the maximum adjusted p-value for large fold changes is 0.05, and that this maximum decreases asymptotically to 0 as the $\log_2$ fold change of 1 is approached (with a curve parameter of one time the overall standard deviation). Proteins consistently significantly differentially expressed through 20 protein imputation cycles were subsequently flagged. Sorting and consequent mass spectrometry experiment was replicated in triplicate (3 WT and 3 *Sca1* animals per replicate). Proteins found in at least 2 replicates experiments were used for PANTHER analysis.

See also Table S1 related to Figure 7. List of identified proteins in adult rodent MLIN.

In vivo two-photon calcium image processing and data analysis

Image analyses were performed in Matlab (R2021a, Math Works) using custom-written routines.[4] In brief, full frame images were corrected for potential x and y brain displacement, and regions of interests (ROIs) were semi-automatically selected based on the maximum and mean projection of all frames. Fluorescence intensity of all pixels within a selected ROI were averaged in each frame, and the resulting time series (traces) low pass filtered at 10 Hz and smoothed over 3 frames. Potential neuropil signal contamination was addressed with the following equation (F_{ROI_comp}, neuropil-compensated fluorescence of the ROI; F_{ROI}, initial fluorescence signal of the ROI; $F_{neuropil}$, signal from the neuropil) (modified after Chen et al.,[19] Liebscher et al.,[93] and Scekic-Zahirovic et al.[94]).

$$F_{ROI\_comp} = F_{ROI} - 0.8 \times F_{neuropil}$$

In case the median of $F_{neuropil}$ was higher than the median of F_{ROI}, we opted for a neuropil compensation factor of 0.7. To estimate the noise and to compute the baseline of each trace (F0), we subtracted the 8th percentile in a sliding window of 30 frames. The standard deviation of this trace divided by its median and after subtracting 1, yields the noise of each trace. F0 corresponds to the median of all values lower than the 70% percentile of the noise band. All further analyses are performed on (F_{ROI_comp}/F0)-1 traces, reflecting the ΔF/F. The activity of dedicated neurons is given as area under the curve (AUC) of the ΔF/F per time unit. To minimize contributions of noise fluctuations to this metric, we only considered values exceeding 2x the noise. 8 Running responsiveness was assessed by randomly circularly shifting the ΔF/F trace with respect to the speed vector 1000 times and computing the ratio of the median ΔF/F during locomotion and during quiet wakefulness and comparing it to the actual activity ratio of a given ROI. Neurons for which the actual 'locomotion/quiet wakefulness' activity ratio exceeded the 95th percentile of the shuffled data were considered running responsive. Spontaneous activity reflects the AUC during quiet wakefulness. Only experiments with a minimum of 4000 frames, corresponding to 2.7 min, were considered in this analysis. Air puff responses were assessed in experiments with at least 2 air puffs,

which were not followed by a running response in a window of 3 seconds following the puff application to avoid crosstalk between modalities. Due to these varying sets of criteria, the effective number of neurons differs across analyses.

Population activity dimensionality and manifold analysis

To reduce the dimensionality, we applied principal component analysis (PCA) to the 0-centered and z-scored ΔF/F traces of all neurons or of selected cell-types in each FOV in the feedback imaging sessions.[27,95] To assess the correlation between the population response pattern and the conjunct recorded behavior, a linear regression was performed for the principal components and the different behavioral parameters, i.e., locomotion, pupil width, whisking and air puff and all measured behavior combined, to separate active from quiescent states. To further explore the structure of the behaviorally associated population response patterns, we conducted a PCA-based manifold analysis by projecting high dimensional population response pattern trajectories into 3 dimensional PCA space. The manifold subspace clearly segregated into two distinct clusters, corresponding to quiet wakefulness and active state (dominated by locomotion). The center of mass for the respective subspaces was computed as the mean of the coordinates within each subspace. The Euclidean distance within a given subspace corresponds to the average length of each dot to the center of mass. The Euclidean distance between two subspaces reflects the distance between the center of mass of each subspace. To compare the Euclidean distances between WT and *Sca1*, only experiments with at least 30% of the time spent being stationary and a minimum of 20% of the time spent running were included. Of note, as the number of ROIs in a given field of view (FOV) varied significantly within the acute chemogenetic stimulation data set, we bootstrapped by subsampling 70 pseudorandomly selected ROIs in each FOV for each of the 100 iterations and computed the mean values of the derived center of mass.

Statistical analysis

Analysis was done using GraphPad Prism and Matlab (R2021a, Mathworks). Statistical significances throughout the paper were evaluated by two-tailed, unpaired Student's *t* test, Two-way ANOVA or Kolmogorov-Smirnov (KS) tests to assess differences in distributions. Post ANOVA Sidak or Tukey test was used to evaluate statistical significance throughout the paper as indicated in the respective figure legend. Values are expressed as mean ± standard error of the mean (SEM). A P-value <0.05 was considered as statistically significant (*p <0.05, **p<0.01, ***p<0.001).

Figure	Test	F / t / R / etc. values
1E–1J	Kolmogorov-Smirnov test	
1N	2-way repeated measures ANOVA	genotype $F_{(1,2092)}$ = 71.89
1O	Wilcoxon rank sum test	
1P	2-way repeated measures ANOVA	genotype $F_{(1,163)}$ = 12.18
1Q	Wilcoxon rank sum test	
1R	2-way repeated measures ANOVA	genotype $F_{(1,250)}$ = 0.17
1S	Wilcoxon rank sum test	
2C	2-way ANOVA	genotype $F_{(1,28)}$ = 2.07
2D–2F	Wilcoxon rank sum test	
3A	Chi-square	
3C–3E	Unpaired t-test	
4B	Chi-square	
4C	2-way ANOVA (Sidak multiple comparison test)	time $F_{(11,192)}$= 9.761, treatment $F_{(1,192)}$= 97.34, interaction $F_{(11,192)}$= 12.35
4H–4O	Kolmogorov-Smirnov test	
4Q	Wilcoxon rank sum test after bootstrapping	
5C	Chi-square	
5D	Two-way ANOVA (Sidak multiple comparison test)	timepoints $F_{(11,180)}$= 10.55, treatment $F_{(1,180)}$= 37.88, interaction $F_{(11,180)}$= 12.09,
5F and 5G	Unpaired t-test	
5I	Two-way ANOVA (Sidak multiple comparison test)	time points $F_{(4,70)}$= 0.9894, treatment $F_{(1,70)}$= 38.49, interaction $F_{(4,70)}$= 1.095
5J	Unpaired t-test	
6B	Chi-square	
6C–6E	Unpaired t-test	

(*Continued on next page*)

Continued

Figure	Test	F / t / R / etc. values
6F	Two-way ANOVA (Tukey multiple comparison test)	timepoints $F_{(4,215)}$=1.030, treatment $F_{(3,215)}$= 28,59, interaction $F_{(12,215)}$= 1.039
7G	Unpaired t-test & Pearson correlation	
7H	Chi-square	
7I	Unpaired t-test	
8A	Unpaired t-test	
8B	Chi-square & Pearson correlation	
8C	Multiple t-test	
8D	Unpaired t-test	
8F and 8G	Multiple t-test	

Table indicating precise statistical test employed for main figures.